



## Article

# Spatiotemporal Variability of Dune Velocities and Corresponding Uncertainties, Detected from Optical Image Matching in the North Sinai Sand Sea, Egypt

Eslam Ali <sup>1</sup> , Wenbin Xu <sup>2,\*</sup> and Xiaoli Ding <sup>1</sup>

<sup>1</sup> Department of Land Surveying and Geo-Informatics, The Hong Kong Polytechnic University, Hong Kong 999077, China; eslam.a.saleh@connect.polyu.hk (E.A.); xl.ding@polyu.edu.hk (X.D.)

<sup>2</sup> School of Geosciences and Info-Physics, Central South University, Changsha 410083, China

\* Correspondence: wenbin.xu@csu.edu.cn

**Abstract:** Understanding the relationship between climatic conditions and dune ecosystems requires the large-scale monitoring of spatiotemporal patterns of dune velocities. Due to their large extent and remoteness, dune fields are ideal for remote sensing techniques. Dune velocities in the Sand Sea North Sinai are characterized by large spatial and temporal variability. To this end, a total of 265 pairs from four Landsat-8 images from April 2013 to April 2018 were automatically matched with the COSI Corr engine to determine the dune velocities. These pairs were selected so that differences in the solar angles were small and spanned at least one year. This helps to reduce shadowing in the deformation fields and the error budget in converting displacements to annual velocities. To improve spatial coverage and reduce measurement uncertainty, the fusion of individual offset maps is considered feasible. We compared the performance of two methods (i.e., inversion and temporal median fusion) in performing the fusion of individual velocities, and the two methods showed good agreement. The fusion of individual velocities allowed us to estimate the final velocities for about 98.8% of the dune areas. Our results suggest that the magnitudes and directions of dune migration at Sand Sea are spatially and temporally variable. The geometric mean of the active features associated with 12 regions in the Sand Sea ranged from 1.65 m/y to 3.52 m/y, with median directions from 56.19° to 173.11°. The stable regions allowed us to estimate the 95% confidence intervals of the final velocities and extend these calculations to the dune targets. The median uncertainties were 0.10 m/y and 0.25 m/y for the stable and moving targets, respectively. We estimated the coherence of the final velocity vector, which can be considered as an indicator of the homogeneity of migration directions between the offset maps. We compared the final Landsat-8 velocities with those from Sentinel-2 to validate the results and found a good agreement in the magnitudes and directions. The process of selecting high-quality pairs and then fusing the individual maps showed a high performance in terms of spatial coverage and reliability of the extracted velocities.

**Keywords:** dune dynamics; dune velocity; feature tracking; Landsat-8; Sentinel-2; COSI-Corr; fusion; uncertainty; wind regimes



**Citation:** Ali, E.; Xu, W.; Ding, X. Spatiotemporal Variability of Dune Velocities and Corresponding Uncertainties, Detected from Optical Image Matching in the North Sinai Sand Sea, Egypt. *Remote Sens.* **2021**, *13*, 3694. <https://doi.org/10.3390/rs13183694>

Academic Editor: Norman Kerle

Received: 17 August 2021

Accepted: 10 September 2021

Published: 15 September 2021

**Publisher's Note:** MDPI stays neutral with regard to jurisdictional claims in published maps and institutional affiliations.



**Copyright:** © 2021 by the authors. Licensee MDPI, Basel, Switzerland. This article is an open access article distributed under the terms and conditions of the Creative Commons Attribution (CC BY) license (<https://creativecommons.org/licenses/by/4.0/>).

## 1. Introduction

Dunes are the most common landforms in terrestrial and extra-terrestrial deserts, where they account for approximately 30% of Earth deserts. The lack of vegetation cover, precipitation, and high temperatures provide an ideal environment for dune reconstruction and formation. Most studies primarily employed site measurements; however, these measurements provided an accurate solution, and they mainly focused on monitoring single dunes and were handicapped by higher times and cost requirements [1]. Scaling measurements obtained from single dunes at a specific time scale to large spatial and temporal domains is considered a problem, especially for studies related to modeling the spatial patterns of dunes [2]. The revolution of remote sensing (RS) techniques since the

1970s opened the doors to the transition from monitoring single dunes to monitoring the dune field scale [1]. The reliance on RS techniques enabled the study of a spatial analysis in relation to various aspects, including dune activities, patterns, dynamics, and dune hierarchies [1]. Changes in climate conditions may lead to the reactivation of stable dunes or the stabilization of active dunes, depending on the changes in wind power, evapotranspiration, precipitation, and vegetation cover [3]. Dune migration poses a significant threat to agricultural lands, water supply pathways, natural and artificial lakes, and transportation networks [4,5]. Studying the status of dune dynamics would help to identify the high-risk areas that should be protected to mitigate their threats, especially desertification [6–10]. Early attempts at RS primarily depended on aerial photos to trace dune migration in several studies; however, aerial photography is considered expensive [1]. The multispectral satellite imagery provides large spatial and temporal coverages with relatively no cost (i.e., the free archives), unlike the filed measurements and aerial photographs, which are mainly constrained by cost. Several platforms were previously employed, including Landsat (4–8) (e.g., [6,7,9,11–16]), Advanced Spaceborne Thermal Emission and Reflection Radiometer (ASTER) (e.g., [17–20]), Systeme Probatoire D’Observation De La Terre (France): SPOT (5–7) (e.g., [21–23]), Worldview (e.g., [24]), and Sentinel-2 (e.g., [7,9,25]) to investigate the different aspects, including dune migration, desertification, and sediment transport pathways. The most common technique that has been widely used to monitor dune migration is measuring the distance between the two lines extracted from two georeferenced images captured at different times, wherein these lines represent dune slip faces [1]. This method primarily provides good spatial coverage with no cost but is handicapped by its reproducibility and applicability and is primarily affected by the satellite geometry, illumination conditions, clouds, and spatial resolution of the images [1]. Some research monitored the volumetric changes of dunes depending on multitemporal DEMs that come from either LIDAR [26–28] or UAVs [29,30]. These multitemporal DEMs would provide accurate information on the rates of erosion and depositions; however, they are handicapped by the cost and limited spatial coverage.

The launch of the Co-Registration of Optically Sensed Images and Correlation (COSI-Corr) by the Caltech group [31] in 2007 provided an alternative to the semi-automatic monitoring of Earth surface deformations (e.g., earthquakes, glaciers, landslides, and dunes). This approach is primarily based on the matching between two orthorectified images, and the correlation is conducted in the frequency domain. In 2008, Vermeesch and Drake pioneered the use of ASTER images together with COSI-Corr to monitor the dune celerity and sand flux of the fastest barchan dunes in the Bode ‘le ’ depression, Chad [18]. They reported the potential of using correlation methods to determine dune migration on a dune field scale. Subsequently, several studies have used COSI-Corr to monitor dune velocities across different dune fields, with different dune morphologies for terrestrial dune fields on different continents, including Africa (e.g., [12,18,21,25]), Asia (e.g., [7,20,32]), and North America (e.g., [19]). In addition, the correlation engine has been used to study extraterrestrial dune fields on Mars (e.g., [33–35]). Previous studies have supported the reliance on the correlation engine of Cosi-Corr as a robust technique characterized by large spatial coverage, less human intervention, and subpixel accuracies up to 1/10th of the ground resolution.

However, as Landsat has only been available since 1972, the studies that employed COSI-Corr have mainly depended on ASTER images (e.g., [2,17,18]) to capture dune migrations. Only one study used Landsat-4 as one of the images used to establish the time series of dune migration over the Sahara Desert [17]. Recently, Baird et al. [12] employed Landsat-5 images together with COSI-Corr to monitor the dune migrations in two dune fields, where they found that the distribution of the ground control points (GCP) used in the orthorectification over sand patches affected the orthorectification accuracy and led to mismatches. More recently, few studies have paid attention to the free archives of Landsat-8 and Sentinel-2 as sources of free satellite images to feed into the correlation algorithm to monitor historical dune migrations [9,25]. Both Landsat-8 and Sentinel-2

have witnessed an enhancement in temporal and radiometric resolutions, orthorectification accuracy, and co-registration accuracy [36,37]. Additionally, both satellites have sufficient orthorectification levels, which enable the direct matching of images [36].

The lack of field measurements and the cost of high-resolution images would further augment the dependency on Landsat-8 and Sentinel-2 as sources to retrieve the annual velocities of dune migration. However, the automation, wherein large spatial coverage is provided by matching measurements, is always exposed to several sources of errors, such as artificial deformations due to casted shadows [38,39], stripe artifacts due to alignment errors in the couple charged device (CCD) [39,40], and mismatches due to the presence of clouds [41]. Due to the filtering process, the dependency on individual matching measurements would be compromised by a low spatial coverage. Consequently, combining the measurements from several offset maps would help keep more velocities and increase the reliability of the final velocity by decreasing the uncertainties [42]. The combination of individual velocities (hereafter called fusion) gained importance due to the availability of the free archives (e.g., Landsat 4/5/7/8, and Sentinel-2) with high temporal resolutions. The fusion of individual velocities is uncommon in dune studies; however, it was previously employed extensively in glacier studies (e.g., [37,42–45]). Dehecq et al. [42] introduced large-scale velocities for glaciers in the Pamir-Karakoram-Himalayas for the period 1999–2001, where they processed 1536 pairs generated from 1382 images belonging to 68 Landsat 5/7 frames and employed a spatiotemporal median to introduce the final velocity. Fahnestock et al. [37] monitored the rapid change in the ice velocities by matching Landsat-8 pairs with short time baselines and then estimated the final velocity by employing the weighted average.

The North Sinai Sand Sea (NSSS) is characterized by a large variability in terms of the migration magnitudes and directions [21,46]. This variability can be attributed to spatial and temporal variations in the wind speed and direction, change in dune sizes, observation period, and technique [21,46]. Due to the variability in dune migration rates, it can be assumed that dunes have different migration magnitudes between comparative measurements. The availability of free archives (e.g., Landsat-8 and Sentinel-2) provides the opportunity to process a high level of redundancy in measurements. Here, we present a workflow that aims to combine individual measurements to represent the spatiotemporal variability and associated uncertainties in dune velocities throughout the NSSS. We introduce a full coverage of dune velocities in the NSSS using the matching results from Landsat-8 and Sentinel-2. First, we automatically select pairs with lower solar angle differences that span at least one year. The selection aims to control the casted shadows, mismatches, and aberrant measurements. The fusion of all matched measurements is promising to reduce the uncertainties and improve the spatial coverage. Thanks to the fusion, we successfully covered about 98.8% of the total area of the Sand Sea. We use the stable regions to establish a relationship between the number of individual velocities used to estimate the final velocity and the corresponding uncertainties. We then use the calibration models to estimate the uncertainties of moving targets. We estimated the coherence of velocity vectors (VVC), which is an indicator of the homogeneity of migration directions between individual matching measurements. Owing to the paucity of the field measurements, we compared the final velocities of Landsat-8 and Sentinel-2, and the comparison showed good agreement. The selection process and the fusion of the individual maps allowed us to capture the spatiotemporal variability of dune movement in the NSSS with higher reliability.

## 2. Study Area and Data

### 2.1. Study Area

The NSSS is located in the northwestern part of the Sinai Peninsula. The Sand Sea occupies an area of about 13,600 km<sup>2</sup> with a sand cover of 12,600 km<sup>2</sup> [46,47]. The Sand Sea is bound on the west by the Suez Canal and on the east by the eastern border of Egypt, on the north by the Mediterranean Sea and on the south by the southern slopes

of the mountains (Figure 1). Two main dune types predominate in the Sand Sea: linear and transverse dunes. In the NSSS, there are three groups, distinguished according to their location: (1) linear and transverse dunes, located in the northern part and oriented east–west due to the prevailing wind direction, (2) the dunes east of the Bitter Lake, which are mainly linear dunes oriented north–south, and (3) the coastal dunes, which extend along the coastal strip [46,47]. The transition between the two primary parts is gradual and distinct. The wind regime is complex, as the wind varies in its speed and direction both temporally and spatially. The effective wind regime in the NSSS (4 m/s), as defined by Reference [48], prevails in the western part of the Sand Sea, and the energy of the wind decreases towards the middle and east [21,46].

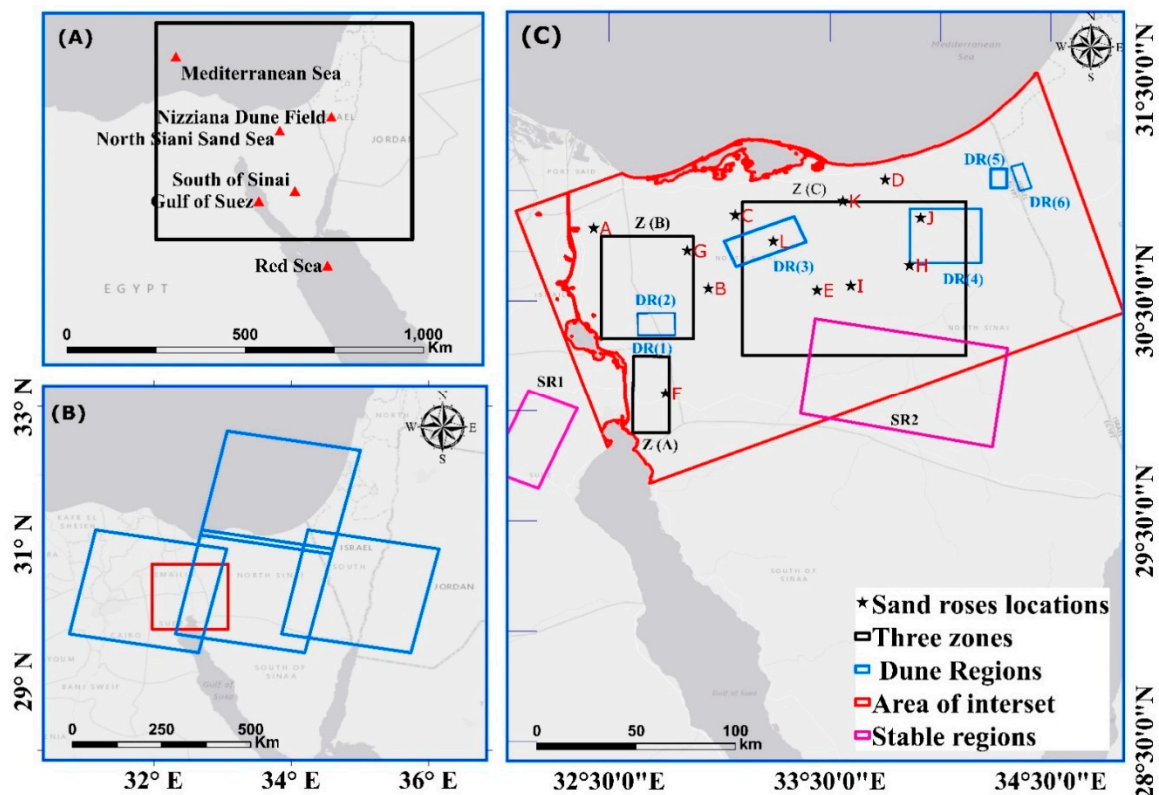


**Figure 1.** (A) Regional map and location of the NSSS. (B) In the black rectangle of (A). The blue and red polygons denote the footprints of Landsat-8 and Sentinel-2, respectively. Panel (C) includes different elements, where the red polygon represents the area of interest used to highlight the final velocity after a combination in Figure 6. The black rectangles denote the zones of interest highlighting the dispersion and uncertainty in Figures 11 and 12. The magenta polygons denote the stable regions used as calibration sites to estimate the uncertainties of the final velocities. The black pentagrams represent the locations where the sand roses in Figure 14 were extracted. The green rectangles display the dune fields used to highlight the spatiotemporal variability in Figure 15. The DR1 coincide with the first zone of uncertainty (Z\_(A)).

### 2.1.1. Optical Images

Landsat-8 level-1T images from four frames (Figure 1B) were used to provide a complete coverage of the dune velocities in the NSSS. Among the different bands of Landsat-8, we mainly used the panchromatic band (band-8; 15-m resolution) as input to the correlation algorithm (COSI-Corr) to determine the displacement. The panchromatic band was chosen to satisfactorily capture the dune displacements at higher resolutions [25]. For cross-validation, we used Sentinel-2 as an independent source to detect the displacements at similar locations.

The Sentinel-2 mission covers the Earth with two satellites, S2A and S2B [36]. The use of both satellites allows for a higher temporal resolution of less than five days at the equator. A NIR image from Sentinel-2 (band-8a) with a spatial resolution of 10 m was used

to produce the displacement maps, as proposed in Reference [25]. The orthorectification level of Landsat-8 and Sentinel-2 is sufficient for monitoring surface deformations, and limiting the matching to the same images can mitigate the effects of orthorectification residuals [36]. Only images with cloud cover less than 10% were used for matching. All the images were downloaded using the bulk download application available on the USGS website (<https://dds.cr.usgs.gov/bulk>, accessed on 12 September 2021). Information on the images used in this study is listed in Table S1.

### 3. Methods

Our workflow shown in Figure 2 includes the following: pair selection, image matching, filtering process, fusion of the individual velocities, and estimation of the uncertainty of the final velocity. The fusion process was estimated depending on two approaches (i.e., inversion and median fusion) to test the sensitivity of these approaches to the results. We discussed two procedures for determining the final velocities: (1) the fusion of the velocities associated with each direction (i.e., east–west (EW) and north–south (NS)) and subsequent application of the Euclidean norm and (2) the application of the Euclidean norm for each offset map and subsequent fusion. The two approaches were compared, and the discrepancies in the final velocities can be attributed mainly to the variability of the migration directions.

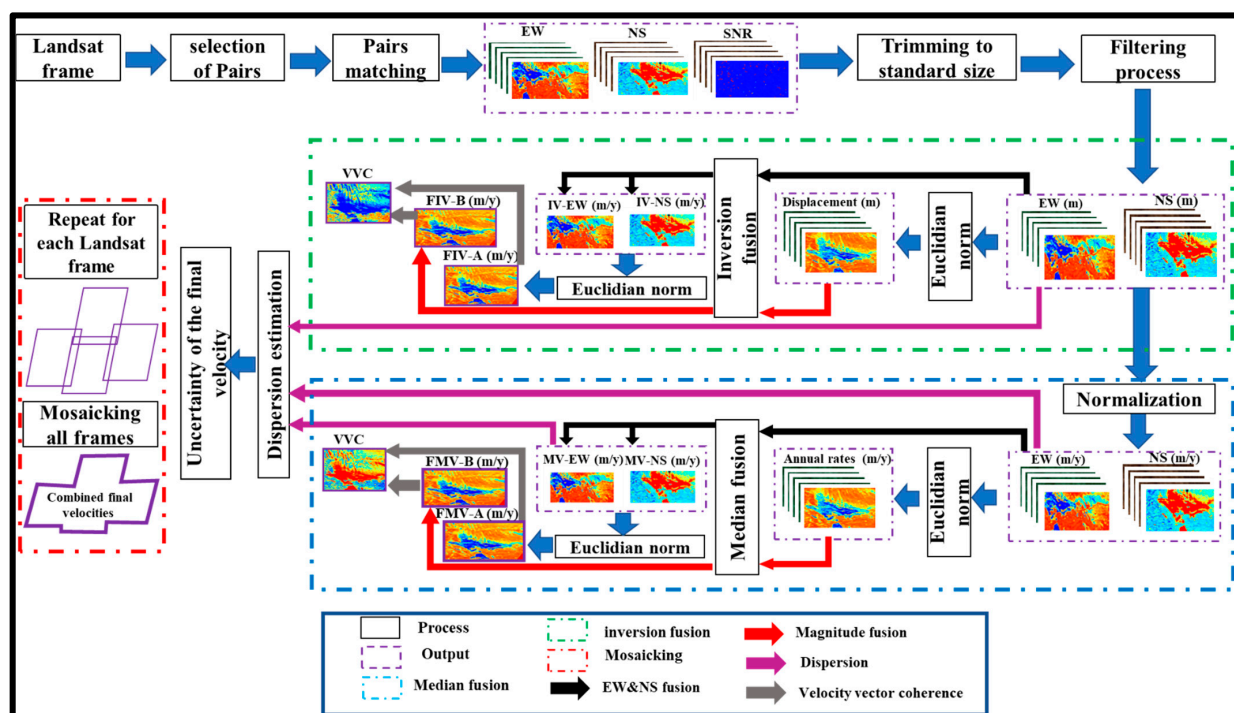


**Figure 2.** The proposed workflow to introduce the full coverage of dune velocities and corresponding uncertainties in the NSSS. The flowchart includes the following steps: (1) pair selection, (2) matching of the selected pairs, (3) the filtering process, and (4) the EW and NS displacement maps (m) were normalized to estimate the annual rates (m/y). The Euclidean norm was applied to estimate the magnitude of the displacement or velocity. Inversion fusion (green dashed rectangle) was used to combine the individual displacement maps into one velocity by inversion. Median fusion (blue dashed rectangle) was used to combine the individual annual rates (m/y) into one velocity. Fusion by either inversion or the temporal median can be performed by two procedures: (1) fusion of the individual displacement components (i.e., EW and NS) and the subsequent application of the Euclidean norm or (2) the application of the Euclidean norm and subsequent fusion. The VVC was estimated to show the homogeneity of the direction extracted from individual offset maps. The flowchart also includes the estimate of the dispersion and the corresponding uncertainties. MV and IV refer to the median and inversion rates, respectively. FIV-B and FIV-A refer to the final inversion velocity by applying the Euclidean norm before and after inversion, respectively. FMV-B and FMV-A are similar to FIV-B and FIV-A but use temporal median fusion.

### 3.1. Pairing Formation and Matching Process

The free archives of optical images (e.g., Landsat-8 and Sentinel-2) provide a large number of images over time for a given study area; therefore, the selection of images to be included in the matching process must be automatic to save time for manual selection [42]. Previous research focused on the time separation as the main control for selecting matched pairs. Dehecq et al. [42] constructed a network around an image with six available images at a time interval of 1 to 2 years. Fahnestock et al. [37] selected pairs with a time interval of 16–96 days to avoid surface changes over time and to monitor the rapid changes in ice velocities. The short time intervals may preserve the surface changes between the two images but increase the likelihood of capturing large portions of the geolocation errors in the deformation fields [37]. The large difference between the solar angles (i.e., solar azimuth and solar elevation) of the matched pairs would lead to cast shadows in the deformation fields and increase the uncertainties [7,25]. The spatial baseline (SB) in the optical image matching domain is less commonly used, while, in the study by Reference [39], it was recommended to limit the SB to less than 200 m to prevent the occurrence of the stripe’s artifacts. Here, we considered both the temporal and radiometric baselines in the selection process to control the error sources before the matching process. First, we selected images with cloud cover less than 10% to control the uncertainties. Second, we limited the solar angle differences of the matched pairs to less than 10° and 9° for Landsat-8 and Sentinel-2, respectively, the spatial baselines to less than 250 m, and selected pairs with temporal intervals of at least one year. The minimum time interval of one year would help limit the effects of the geolocation errors when converting the displacement to annual velocities, as recommended by References [42,49]. The maximum temporal baselines were set to 4 and 3 years for Landsat-8 and Sentinel-2, respectively. We designed an experiment to investigate the effect of time separation on the matching results, comparing the mean absolute deviation (MAD) of the matching measurements with the stable regions (see Section 4.2). Table 1 summarizes the number of selected pairs belonging to each frame, the observation period, and the baselines of the selection.

**Table 1.** Descriptions of the satellite images and the baselines of the matching pairs used in this study.

Sensor	Frame (Path/Row)	Pairs/Images	Observation Period	Baselines			
				SED (°)	SAD (°)	TS (Yr.)	SB (m)
L8	176/39	113/52	4/9/2013– 3/26/2018	10	10	1–4	250
	175/39	46/30	7/11/2013– 6/7/2018				
	175/38	31/33	6/25/2013– 3/3/2018				
	174/39	70/46	5/1/2013– 4/13/2018				
S2	TR36VU	51/30	12/21/2015– 2/13/2019	9	9	1–3	–
	T36RXV	53/40	20/8/2015– 22/12/2018				

SB: Spatial baseline, TS: Time separation, SED: Sun elevation difference, and SAD: Sun azimuth difference.

An automatic correlation engine in the frequency domain (COSI-Corr) was used for matching between image pairs. The matching was conducted automatically by the batch processing provided by the algorithm. The size of the initial search window, the size of the final search window, the step size, and the number of iterations were specified for each pair and prepared in a specific format. In this case, initial window sizes of 128 × 128 and 64 × 64 were used for Landsat-8 and Sentinel-2, which were reduced down to final window sizes of 64 × 64 and 32 × 32, respectively. Using a step size of 4 and 6 for Landsat-8 and

Sentinel-2, respectively, we obtained displacements in the EW and NS directions, along with the corresponding signal-to-noise ratios (SNRs) at a resolution of 60 m for Landsat-8 and Sentinel-2.

### 3.2. Noise Filtering and Post Processing

The deformation fields always include mismatches, which should be discarded reasonably to capture the actual deformations. However, since the selection criteria aim to reduce the sources of error, there are still some residuals in the deformation fields. The filtering process passes through several stages. First, the outliers are removed, according to the following steps: (1) removing pixels with displacements outside a certain range based on the information about the window size and the maximum expected displacements [7,25] and (2) removing pixels with lower SNR values as a complementary step to filter out the outliers. Wise selection of the SNR threshold should be considered to ensure a balance between spatial coverage and mismatch removal. Removing pixels with lower SNR values may preserve mismatches and discard the correct results [50]. We investigated the relationship between the SNR threshold and the MADs of stable regions, as well as the success rates (SR) for moving targets [50] (see Section 4.1). After discarding the outliers, we removed the orbital residuals that came from the co-registration and orthorectification residuals by performing a polynomial fit [39]. We applied nonlocal mean filtering to preserve fine details and reduce the effects of white Gaussian noise [51]. Finally, the EW and NS filtered displacements were normalized to annual migration by normalization [19].

### 3.3. Fusion of Individual Velocites

To better capture reliable and representative velocity measurements, the combination of a group of deformations into a single velocity is common practice. Here, we compared the performance of two fusion methods in capturing the final velocity representing the average annual rates at the dune field scale. The first is the least squares inversion of the displacements (m) based on Equation (1). The second is applying the temporal median fusion after normalizing the displacement into annual velocities (m/y) based on Equation (2). To enhance the spatial coverage, the fusion was performed pixel by pixel, whereas pixels with a presence level greater than a certain threshold were considered in the fusion process. We also tested the sensitivity of two procedures for estimating the final velocity, as shown in Figure 2. First, we combined the EW and NS maps into two single velocities and subsequently retained the final velocity by calculating the Euclidian norm. Second, we calculated the Euclidian norm of each individual offset map and then combined all the annual rates into a final velocity. The comparison between the two velocities (i.e., applying the Euclidian norm before and after the fusion) highlighted the effect of the variability of the velocity directions.

$$\bar{V}_I(i, j) = (A^T A)^{-1} A^T D \quad (1)$$

$$\bar{V}_M(i, j) = MED\left(V_{(i,j,t)}\right) \quad (2)$$

where  $\bar{V}_I(i, j)$  is the final velocity (m/y) estimated by the inversion,  $A$  is a  $M \times 1$  matrix that includes the time separation between the master and slave of each pair, and  $D$  is the displacement (m) of each individual map.  $\bar{V}_M$  is the final velocity (m/y) obtained by applying the temporal median fusion of the number of  $N$  velocities  $V_{(i,j,t)}$ . The symbols  $-1$  and  $T$  denote the inverse and the transpose, respectively.

After the fusion of individual velocities, we separately mosaicked the fused EW and NS velocities of all the Landsat-8 frames. The velocity mosaics of the two directions (i.e., EW and NS) were used to estimate the final velocity magnitudes and directions across the NSSS.

### 3.4. Uncertainty Estimation

Uncertainties can be defined as factors that affect the matching algorithm and lead to mismatches [38,42]. There are two types of uncertainties: first, the uncertainties of the

individual matching results, and second, the uncertainties in combining the individual results to obtain the final velocity [42]. The individual uncertainties arise from various sources, such as the temporal variation of the surface, the presence of clouds and shadows, and the co-registration of images [38,42]. The uncertainties of the combined velocities are mainly affected by the number of pairs used in the fusion process [42]. Several studies relied on the stable regions to represent the uncertainties of the mismatches or the solution, since it is assumed that the true velocity is close to zero [38,42]. Usually, the uncertainties are represented by the standard deviation; however, it is known that the standard deviation overestimates the uncertainty level [42,49]. Reliance on the median, which is a statistical measure of uncertainty representation, is considered effective, because it is less influenced by outliers [42]. Notably, the uncertainties of the stable targets may not be representative of the overall deformation targets due to the heterogeneous patterns in the moving targets [52]. Dehecq et al. [42] estimated the final velocity uncertainties for both the stable and moving targets. Similar to the study of Dehecq et al. [42], we used the stable regions as calibration sites to establish a relationship between the number of pairs involved in generating the final velocity  $N$ , the dispersion  $\sigma(i, j)$ , and the 95% confidence interval  $CI_{95}(i, j)$ . The 95% confidence intervals of the two components (i.e., EW and NS velocities) are assumed to follow a similar pattern to that of the normal distribution [42], with some variations in the factors governing the equation of the normal distribution, as shown in Equation (3).

$$CI_{95}(i, j) = k \frac{\sigma(i, j)}{N^\alpha} \quad (3)$$

where  $CI_{95}$  is the difference between the 97.5th and the 2.5th quantiles of the final velocity.  $N$  is the number of pairs shared in the estimation of the final velocity.  $k$  and  $\alpha$  are the two factors to be determined.

By changing the number of individual pairs  $N$ , the 95% confidence interval  $CI_{95}(i, j)$  can be estimated for each corresponding  $N$ . To determine the two factors  $k$  and  $\alpha$ , a linear relationship was constructed by applying the logarithm based on Equation (4), where the two parameters can be estimated by least squares linear fitting.

$$\text{Log}\left(\frac{CI_{95}}{\sigma}\right) = a_0 + a_1 * \text{Log}(N) \quad (4)$$

After linear regression, Equation (4) can be applied to estimate the  $CI_{95}(i, j)$  of each velocity component at each valid location. To increase the number of pairs shared in the calibration process, we trimmed parts of the stable region belonging to the overlap region between the two frames (P/175, R/39) and (P/176, R/39) from both the EW and NS velocities. We iteratively changed the number of individual pairs starting from a minimum of five, which was subsequently increased by a factor of two. For each step, we estimated the 95% confidence interval and the dispersion of the records. We then fitted the datasets to Equation (4) to estimate the parameters of each component.

### 3.5. Quality Assessment and Validation

The paucity of in situ measurements of dune velocities hinders the assessment of the quality of extracted velocities [42,49]. Therefore, we depended on several procedures to evaluate the consistency of the results regarding the magnitude and directions. The quality assessment indicators are as follows:

- I. The SR can be defined as the percentage of valid matching results on the sand dune areas. SR can be estimated by calculating the number of surviving pixels over a certain area before and after applying a certain filter [42]. We mainly used the SR to compare the performance of the SNR threshold variations on the percentages of valid matches (Section 4.1).
- II. The dispersion of the final velocity is  $\sigma(i, j)$ ; dispersion is considered the measure of the difference between the estimated final velocity and all the velocities shared in

generating the final velocity [42]. The dispersion can be estimated at each velocity location from Equation (5):

$$\sigma(i, j) = 1.483 \times MED_{n_{min}}^N (|V(i, j, t) - \bar{V}(i, j)|) \quad (5)$$

where  $\sigma(i, j)$  represents the dispersion of the final velocity.  $MED$  is the median of the absolute difference between each individual velocity shared to generate the final velocity and final velocity.  $N$  is the total number of pairs shared in generating the final velocity in the fully stacked pixels, and  $n_{min}$  is the minimum number of pairs required for a given pixel to be considered in the final velocity estimation.

III. The velocity vector coherence of the final velocity is denoted by  $VVC_{(i,j)}$ , where the  $VVC$  is estimated for the final velocity map, representing the change in directions between the individual velocities at each velocity location [42,52]. The  $VVC_{(i,j)}$  can be estimated from Equation (6):

$$VVC_{(i,j)} = \frac{\| \sum_{n_{min}}^N EW(i, j, t), \sum_{n_{min}}^N NS(i, j, t) \|}{\sum_{n_{min}}^N \| EW(i, j, t), NS(i, j, t) \|} \quad (6)$$

where  $\| \|$  denotes the Eculidian norm. The numerator in Equation (6) can be estimated at any velocity location by summing the individual velocities  $EW$  and  $NS$  and then applying the Euclidean norm. Conversely, the denominator in Equation (6) can be estimated by estimating the Euclidean norm of the two components of the velocities (i.e.,  $EW$  and  $NS$ ) and then summing the values of all the included velocities. According to the triangle inequality,  $VVC_{(i,j)}$  ranges from 0 to 1, equals 1 when the directions used in estimating the final velocities are perfectly aligned, and approaches 0 when the directions are heterogeneous [42,52]. We cross-validated the Landsat-8 fusion velocities with Sentinel-2 independent fusion velocities at the overlapping locations. We also compared the final velocities extracted from the overlapping regions of adjacent Landsat-8 images. Cross-validation was performed with respect to the distribution of velocity changes between two sensors and the degree of correlation between the results at similar locations.

### 3.6. Dune Migration Directions

The final velocities  $EW$  and  $NS$  were used to estimate the direction of dune migration with respect to the north based on Equation (7). To better highlight the variability in dune magnitudes and directions, we extracted sand roses from different locations in the NSSS. We clipped a small region (5 km  $\times$  5 km) around each point (Figure 1) and then refined the observations to discard pixels with velocities less than 0.5 m/y, low  $VVC$  (0.65), and higher dispersion ( $>1.5$  m/y). To better estimate the average direction of the group of observations, we should consider that angles with records around  $0^\circ$  and  $360^\circ$  are both oriented to the north. Therefore, using a simple arithmetic mean would be misleading in estimating the average angles. Accordingly, we estimated the average direction for the surviving pixels of each region based on Equation (8). We estimated the concentration ratio (CR) to represent the degree of homogeneity of a group of observations, as suggested in Reference [12]. The CR can be estimated from Equation (9):

$$\theta = \text{atan} \left( \frac{\overline{EW}}{\overline{NS}} \right) \quad (7)$$

$$\bar{\theta} = \text{atan} \left( \frac{\sum_{i=1}^{i=n} (\sin\theta_i)}{\sum_{i=1}^{i=n} (\cos\theta_i)} \right) \quad (8)$$

$$CR = \frac{1}{n} \sqrt{\left[ \sum_{i=1}^{i=n} (\sin\theta_i) \right]^2 + \left[ \sum_{i=1}^{i=n} (\cos\theta_i) \right]^2} \quad (9)$$

where  $\theta$  is the migration direction at each velocity location,  $\overline{EW}$  and  $\overline{NS}$  are the final velocities in the east–west and north–south directions, respectively.  $\overline{\theta}$  is the average direction, and  $CR$  is the degree of concentration, where the  $CR$  ranges from 0 to 1.

## 4. Results

### 4.1. Selection of SNR Thresholds

Figure 3 shows the relationship between the SNR threshold and MAD of measurements belonging to stable areas and the SRs of the surviving pixels from moving targets. We examined the relationship between the variation of the SNR threshold at each 5% step and the MAD measurements for all Landsat-8 pairs in both the EW and NS directions. It can be observed that the maximum value of MAD was about 0.8 m, with a corresponding SNR threshold of 97.5%, before reaching the lower limit of 0.2 m. Conversely, the SRs showed similar trends, with an upper limit of almost 90% with a corresponding SNR threshold of 98%; after which, the SRs started to decrease. These results highlight that choosing an SNR threshold of 97.5% would provide good spatial coverage with lower uncertainties. These results are highly supported by the previous findings of Dehecq et al. [42], who reported similar trends in the relationship between the MADs, SRs, and SNR thresholds. However, the MAD values reported by Dehecq et al. [42] reached an upper limit of 8 m in stable regions, revealing the improvement in the co-registration accuracy of the Landsat-8 archives compared to the earlier Landsat archives (5/7). Here, the SNR threshold was set to 95% for all the pairs included in the study.

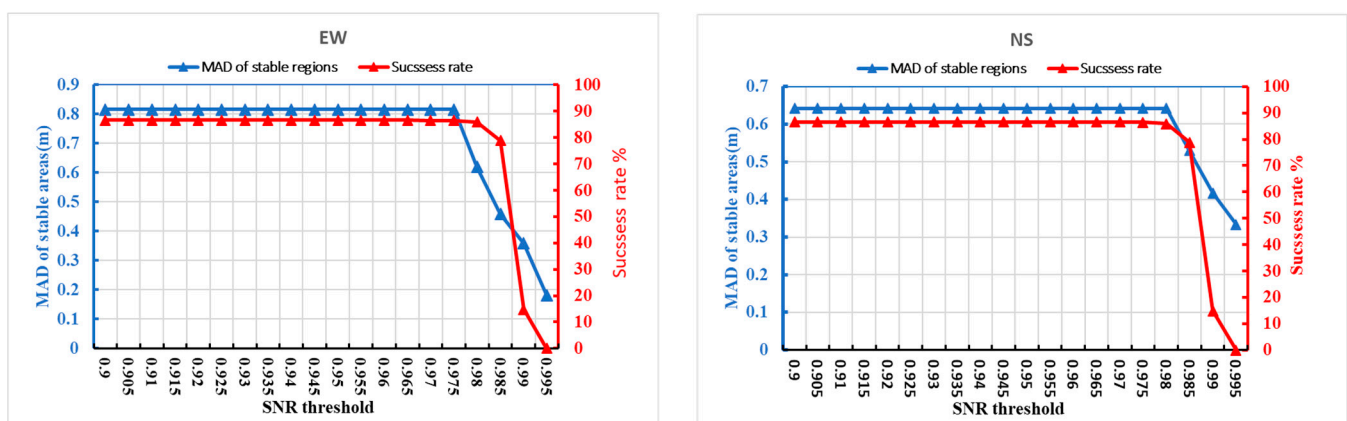


**Figure 3.** The relationship between the SNR threshold and MAD of stable records (blue axis) and between the SNR threshold and SRs (red axis) for EW (left) and NS (right).

### 4.2. Matching Quality vs. Time Separation

Notably, determining an appropriate temporal separation of matching pairs is considered a dilemma. Choosing short temporal intervals to avoid surface changes over time has been strongly recommended (e.g., [2,37]). Conversely, short temporal separation would increase the proportion of geolocation errors in the recorded deformations [42,49]. Here, we compared pairs with different time separations between 32 and 1472 days with the same master image (2/11/2014) in terms of the MAD of stable targets (Table 2). It can be observed that the MAD of the stable areas, which are indicators of the geolocation errors, increased drastically with the decreasing time interval. Notably, for pairs with a duration of at least one year and longer, the values of MAD were less than 0.5 m/yr. This argued for the selection of pairs with a time interval of at least one year, which is also consistent with the previous recommendations by References [42,49]. The maximum temporal spacing should be related and connected to the spacing between dunes [2], nature of migration in the area under consideration [2], and the window size used in the correlation process [2,7,25]. However, short temporal separation would be valuable to monitor targets with higher velocities (e.g., [37]) or to capture seasonal trends in surface deformations.

**Table 2.** The MAD of stable targets for different time separations (same master was used with different slaves).

Pair ID	Master	Slave	TS (Days)	MAD of Stable Targets (m/y)
1		3/15/2014	32	4.44
2		3/31/2014	48	3.74
3		4/16/2014	64	3.42
4		5/18/2014	96	3.61
5	2/11/2014	3/2/2015	384	0.32
6		3/4/2016	752	0.20
7		10/14/2016	976	0.18
8		12/17/2016	1040	0.18
9		2/3/2017	1088	0.13
10		2/22/2018	1472	0.10

#### 4.3. Fusion of Individual Velocites

Figure 4A,C shows the final velocity obtained by applying inversion and median fusion, respectively. Fusion was performed for each direction, and the Euclidean norm was applied. Figure 4B,D shows similar results to A and C, respectively, where the Euclidean norm was applied to each map before fusion. The final velocity was determined for each valid location, combining the fully stacked pixels directly and considering the partially stacked pixels with the least number of pixels in the fusion. The minimum number of individual pairs to be considered as one pixel in the fusion was set to 0.45 times its size, corresponding to a minimum number of 18 pairs. To better assess the sensitivity of the different fusion methods, we extracted the histogram of the absolute differences between the inversion and median fusions, as shown in Figure 5A. It can be observed that the differences had a median of 0.06 m/y, showing the similarity of the extracted velocities regardless of the fusion method. However, median fusion showed slightly higher values than inversion fusion. In addition, we compared the differences between the application of the Euclidean norm before and after fusion for both fusion methods, where the medians of the absolute differences were 0.33 and 0.27 m/y for inversion and median fusion, respectively. Notably, the difference between the application of the Euclidean norm before and after fusion is considered indicative of the variability in the velocity directions between the individual maps.

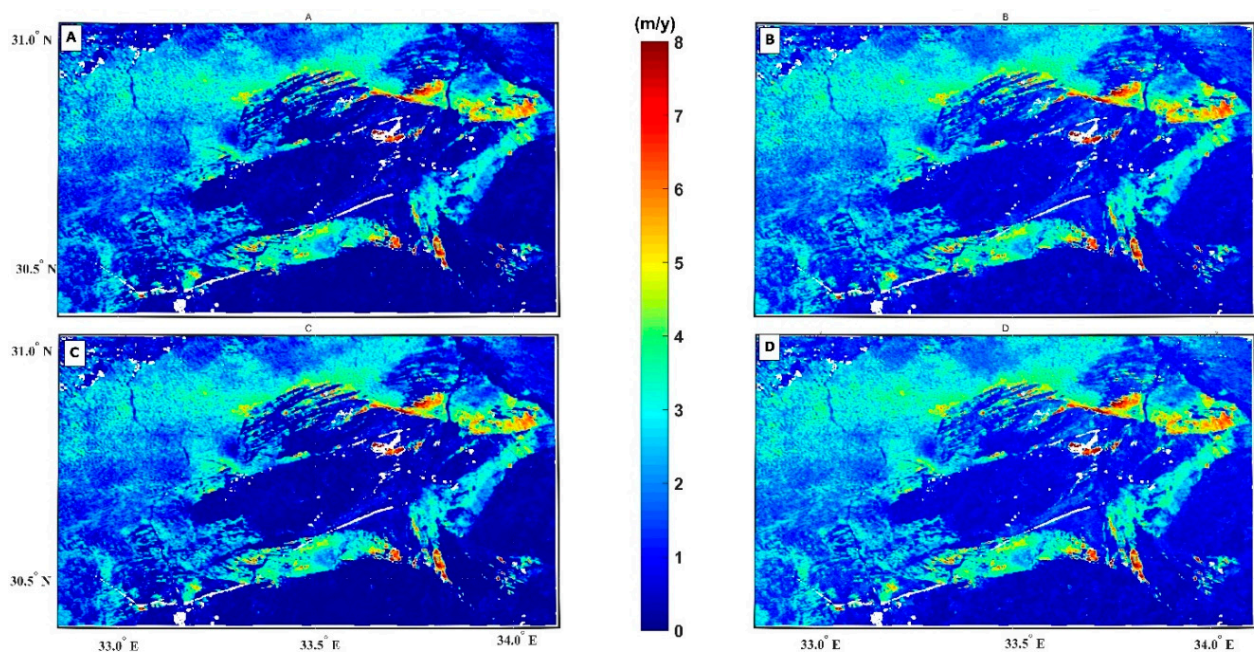
#### 4.4. Mosaicking of Final Velocity Fields

Figure 6A,B shows the combination of final velocities extracted from the four Landsat-8 frames representing the final NSSS dune velocities through inversion and median fusion, respectively. It is noteworthy that the fusion process was performed after converting the images into a common UTM zone, while we used the UTM 36N zone as a common projection frame. It is worth noting that mosaicking the final velocities for such small regions as this sand sea would not pose a problem in unifying the joint projection compared to mosaicking a large number of individual images (e.g., the 68 individual images in the study by Dehecq et al. [42]). Thanks to the fusion, we were able to successfully estimate the dune velocities for about 98.8% of the dune areas. Mosaicking was performed by merging the images depending on the overlapping regions, where we compared the dispersion values at the overlapping locations; pixels with lower dispersions were weighted highly in the mosaicking. The maximum annual migration rates were 14.10 and 14.85 m/y for inversion and median fusion, respectively.

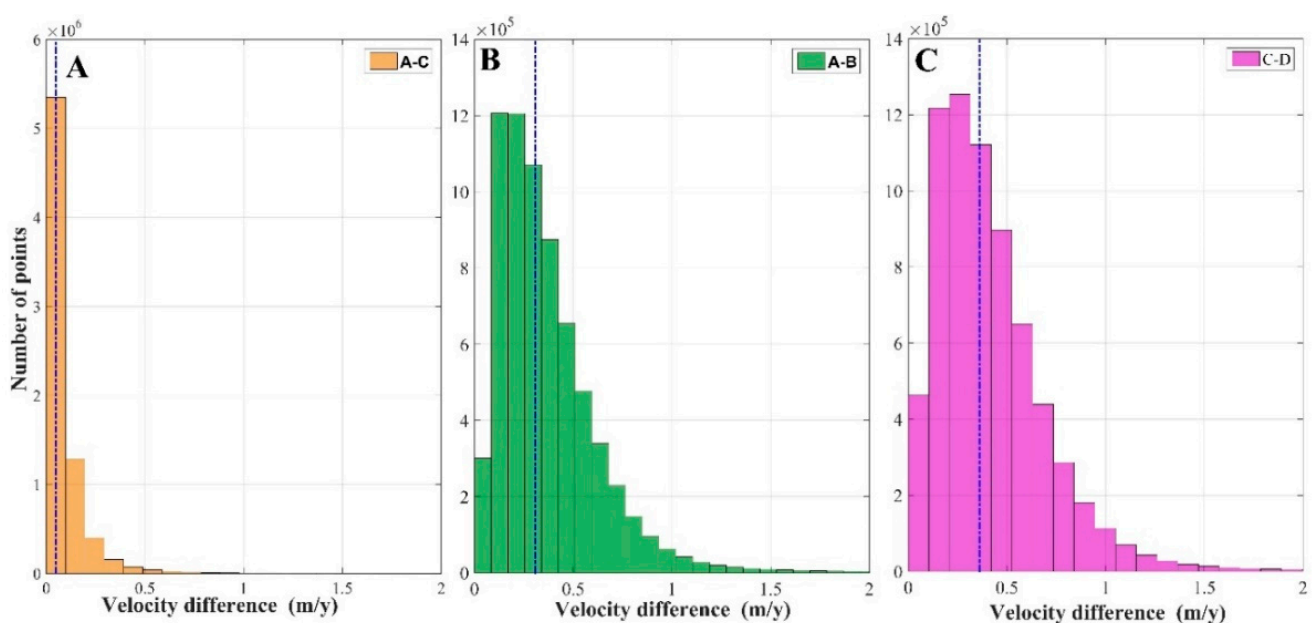
#### 4.5. Cross Validation

Figure 7 shows the relationship between the final velocities extracted from neighborhood Landsat-8 frames at common locations. Of note is the good agreement between the measurements in the overlapping areas with Pearson correlation coefficients of 0.86 and 0.89 between path/row 175/38 and 175/39 and path/row 175/39 and 176/39, respectively.

The histogram of absolute differences of the final velocities between overlapped ping frames is shown in Figure 7C, where the medians of the absolute differences were 0.28 and 0.29 m/y between path/row 175/38 and 175/39 and those of path/row 175/39 and 176/39, respectively. This good agreement between the velocities from neighboring frames demonstrates the potential of the filtering techniques applied to all the individual maps and the sufficient orthorectification levels applied to the new Landsat-8 mission for the frames covering our study area.



**Figure 4.** Final velocity comparisons. (A) The final velocity of dune migration, where the final velocity was estimated by first conducting the inversion of each component separately and then estimating the Euclidian norm. (B) The final velocity by inversion but by estimating the Euclidian norm of each individual map before inversion. (C,D) Similar to (A,B), where the fusion was conducted by the temporal median. The white background denotes the pixels with Nan values.



**Figure 5.** Histogram of the absolute velocity differences between the different procedures employed to retain the final velocity. (A) difference between (A) and (C) in Figure 4. (B) Difference between (A) and (B) in Figure 4. (C) Difference between (C) and (D) in Figure 4. The dashed blue lines represent the median values.

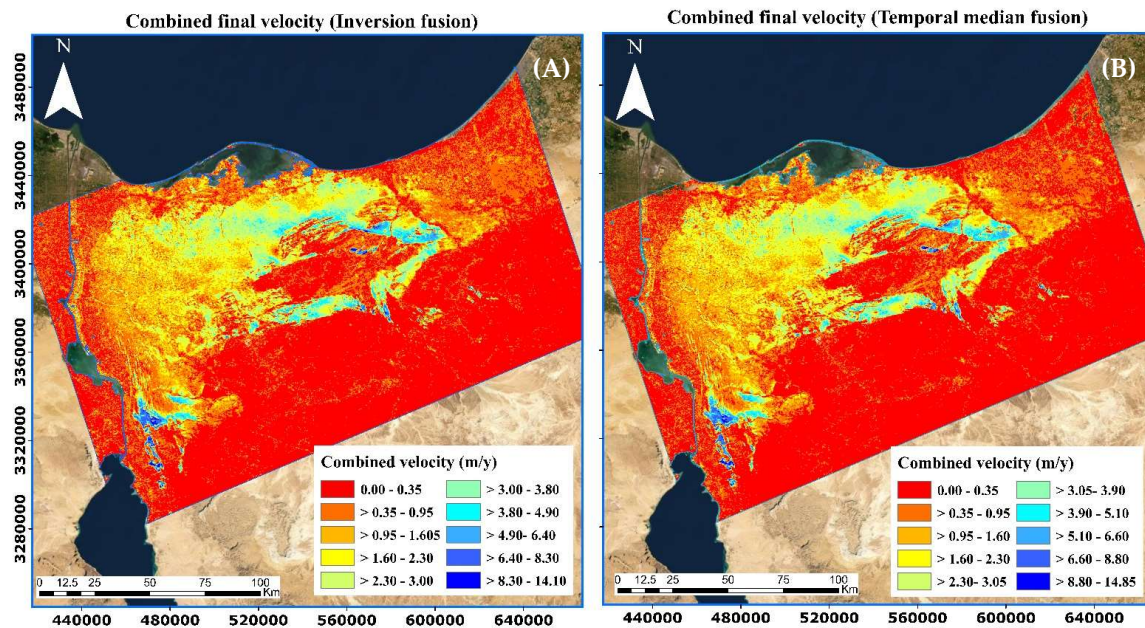


**Figure 6.** The mosaicked final velocity by inversion (A) and by median fusion (B). The blue shapefile is the area of interest focusing on the North Sinai Sand Sea. The water bodies were removed using the blue shapefile. The mask was generated by intersecting the area of interest with the water bodies provided with ASTER GDEM version 3 ([https://gdemdl.aster.jspacesystems.or.jp/index\\_en.html](https://gdemdl.aster.jspacesystems.or.jp/index_en.html), accessed on 12 September 2021). The reference projection used is the UTM projection zone 36 N. The background is Google Earth Image © using Esri ArcMap 10.3.

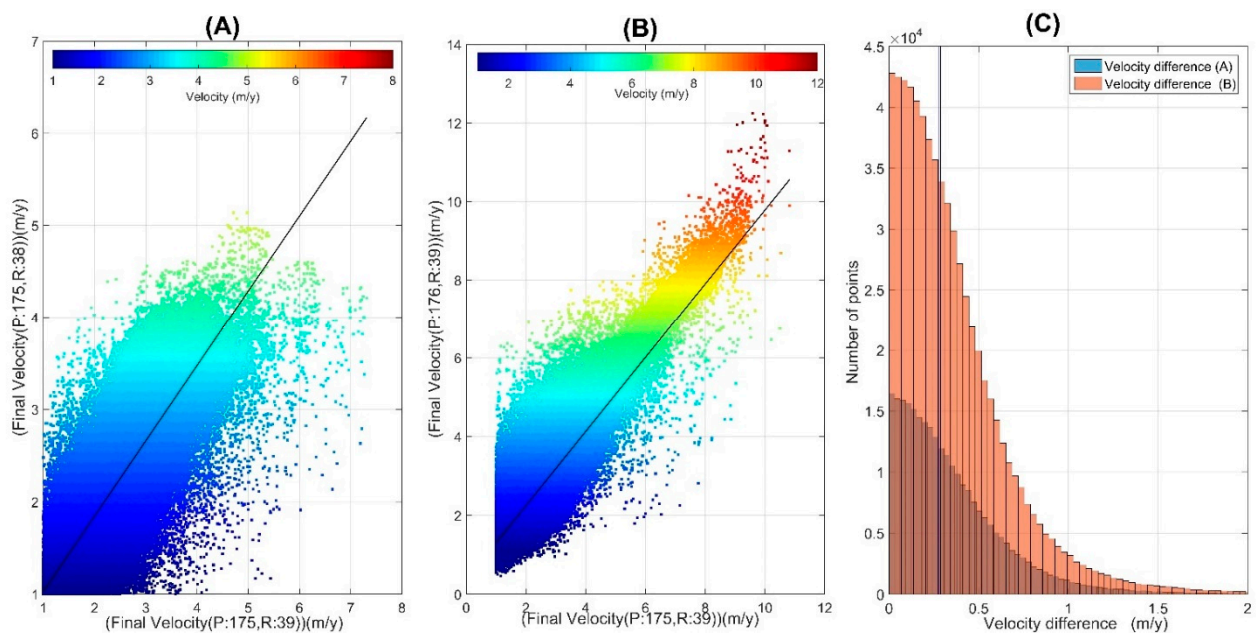


**Figure 7.** Cross-validation of the velocities at the overlapping areas of neighboring Landsat frames at the common locations. (A) The relationship between the final velocity extracted from the two frames (P/175, R/39) and (P/175: R/38). (B) The relationship between the velocities extracted from the two frames (P/175, R/39) and (P/176, R/39). (C) The histogram of the absolute velocity differences between each comparable velocity in (A) and (B).

The spatial gradients were already noted in the study by Baird et al. [12] between the neighboring frames of Landsat-5, where the differences between the velocities of the

overlapping frames were attributed to a poor orthorectification performance. This was mainly due to the poor distribution of GCPs used for orthorectification, as most GCPs were over sandy areas. Baird et al. [12] also reported that Landsat frames covering only sandy features without extensions of the stationary reference points were more prone to orthorectification errors. Following the previous discussion, we agreed with previous reports on the improvement of Landsat-8 orthorectification accuracy [36]. However, our study area has a good extent in stable targets (i.e., mountains), which provides good orthorectification accuracy. A detailed study of the orthorectification performance and distribution of GCPs should be considered for Landsat-8 and Sentinel-2, especially for imagery covering only moving targets, as recommended by Baird et al. [12].

In the second step of cross-validation, we performed a comparison between the two interdependent solutions of the two sensors (i.e., Landsat-8 and Sentinel-2). Figure 8 shows the relationship between the two Landsat-8 frames ((P/175, R/39) and (P/176, R/39)) and the Sentinel-2 frame (TR36VU) at the overlapping locations. The Pearson correlation coefficients were 0.85 and 0.89 between (P/176, R/39) and (TR36VU) and between (P/175, R/39) and (TR36VU), respectively. The medians of the absolute velocity differences were 0.50 m/y and 0.42 m/y between (P/176, R/39) and (TR36VU) and between (P/175, R/39) and (TR36VU), respectively. It is noted that the medians of the absolute differences between the overlapping Landsat-8 frames were smaller than those of the absolute velocity differences between the Landsat-8 and Sentinel-2 frames. This can be considered reasonable and acceptable due to the different observation periods of the different sensors. The comparison of the velocity directions extracted from the different sensors is discussed in Section 4.4.

**Table 3.** The parameters of the least squares regression of the relationship between the ratio  $\text{Log} \left( \frac{CI_{95}}{\sigma} \right)$  and the number of individual velocities shared in estimating the final velocity.

Component	$k$	$\alpha$	$r$
EW	3.10	0.56	0.99
NS	2.40	0.47	0.97

#### 4.6. Uncertainty of Final Velocities

In this section, we describe the dispersion and corresponding uncertainties of the final velocities, focusing on the three zones shown in Figure 1C (black polygons) as follows: the first zone lies east of the Suez Canal (32.60°–32.75° E, 29.90°–30.20° N), the second zone lies east of Bitter Lake (32.5°–32.7° E, 30.45°–30.70° N), and the third zone lies between the two mountains (i.e., Gabel El Maghara and Gabel Yelleq; 33.2°–34.1° E, 30.4°–30.8° N). Figure 9 shows the dispersion of the final velocities in the three regions estimated by Equation (2). We estimated the medians of dispersion of the first two regions (over moving targets) for pixels with velocity values greater than 0.5 m/y. The medians of the dispersion were 0.58 m/y and 0.64 m/y for regions 1 and 2, respectively. In addition, the extracted medians of the dispersion in stable regions 1 and 2 were 0.12 m/y and 0.14 m/y, respectively.

Uncertainty in the final velocity was estimated as a function of dispersion and the number of individual velocities included in the final velocity estimate. The number of pairs included in the final velocity estimate ranged from 46 to 113 for the first two regions, while the third region belonged to the frame (P/175, R/39); the number of individual maps ranged from 18 to 46. Figure 10 shows the linear relationship between  $\text{Log} \left( \frac{CI_{95}}{\sigma} \right)$  and  $\text{Log} (N)$  with a high degree of correlation (see Table 3). It is noteworthy that the relationship is affected by the small number of individual pairs, because when the number of offset maps is smaller (e.g., 5), the median is more prone to misestimation due to the deviation from the normal distribution [42]. In line with the previous discussion, and because the threshold for the minimum number of individual pairs required to consider a given pixel in the fusion process was around 18, we discarded the points with a minimum

number of less than 10 and then estimated the regression parameters, which are shown in Table 3.

Figure 11 shows the spatial variability of the uncertainty of the final velocities in the three previous regions. It can be observed that the uncertainty reflects the same dispersion patterns, weighted by the number of individual velocities involved in the generation of the final velocity. Figure 12 shows the uncertainty distribution for the stable regions and the moving targets for Landsat-8 and Sentinel 2. For Landsat-8, the median uncertainties of the stable targets were 0.07 and 0.08 m/y for stable regions 1 and 2, respectively. The median uncertainties of the active dune areas were 0.25 and 0.24 m/y for regions 1 and 2, respectively. For Sentinel-2, the median uncertainties of the dune areas were 0.19 and 0.15 m/y for regions 1 and 2, respectively. For stable region 1, the estimated median uncertainty of Sentinel-2 was 0.04 m/y. Notably, the uncertainty of moving targets over the same regions had lower values in Sentinel-2 than in Landsat-8, which can be explained by the lower spatial resolution of Sentinel-2 (10 m) compared to Landsat-8 (15 m). A comparison of our records of the median uncertainties over stable regions with those of Dehecq et al. [42] showed that the uncertainties we extracted from the Landsat-8 fusion were only 5%, while the median uncertainties were 2.0 m/y, which can be considered as an indicator of the improvement of the co-registration accuracy of the Landsat-8 archives compared to the previous Landsat archives (5/7). Furthermore, the comparison showed the potential of the pairs selection and filtering procedure employed for the matching results.

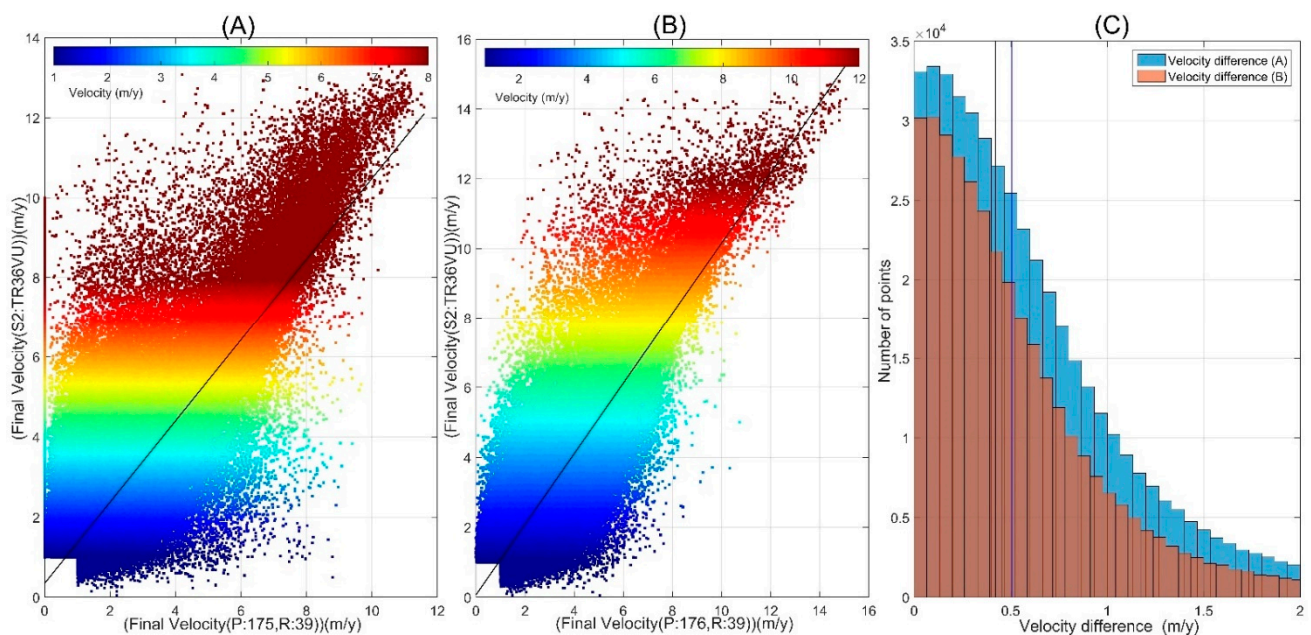
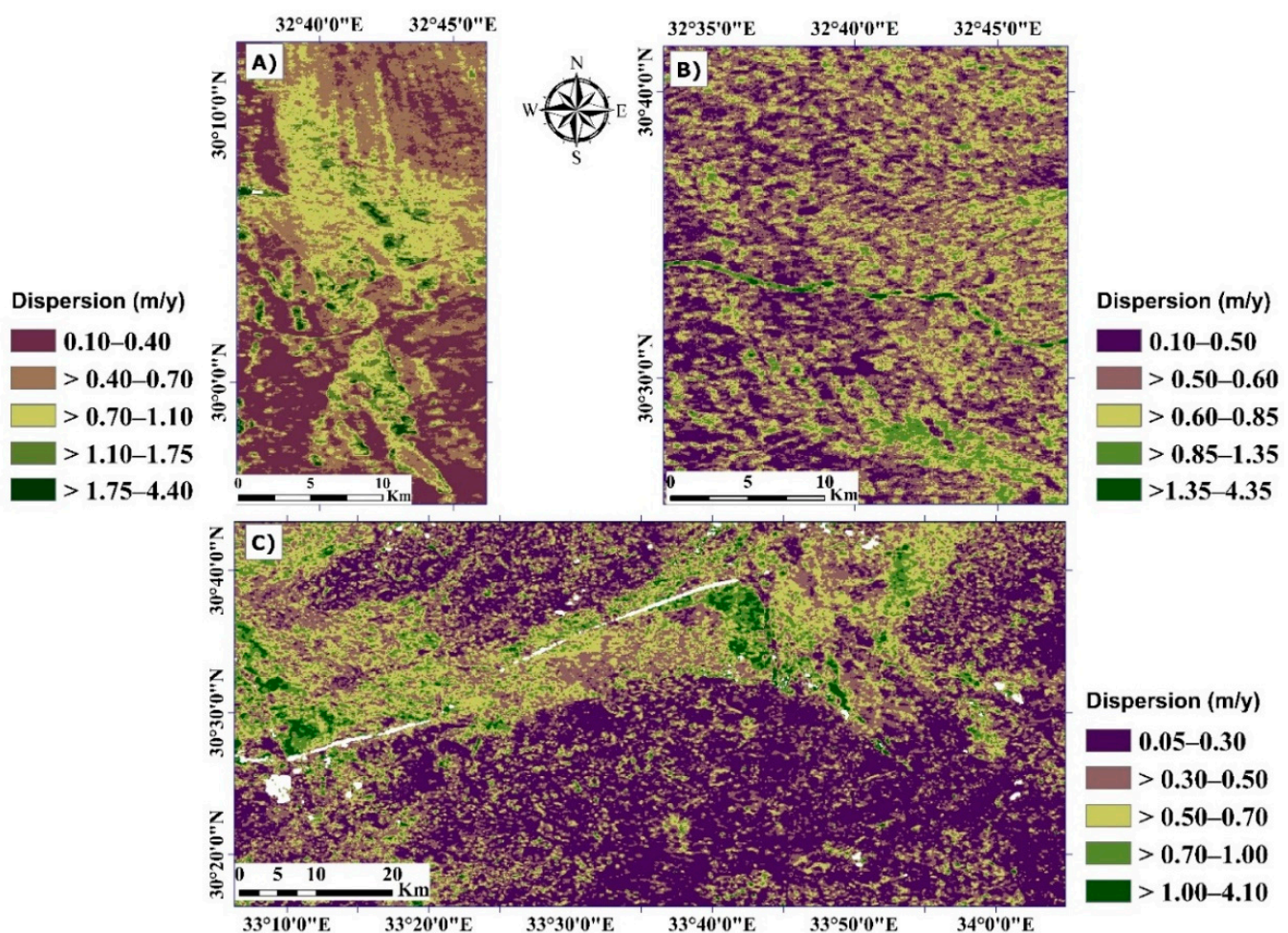


**Figure 8.** Cross-validation of the velocities at the overlapping areas between the Landsat and Sentinel-2 frames. (A) The relationship between the final velocities extracted from the Landsat-8 (P/175, R/39) and Sentinel-2 (TR36VU) frames. (B) The relationship between the final velocity extracted from the Landsat-8 frame (P/176, R/39) and Sentinel-2 (TR36VU). (C) The histogram of the absolute velocity differences between each comparable velocity in (A) and (B).

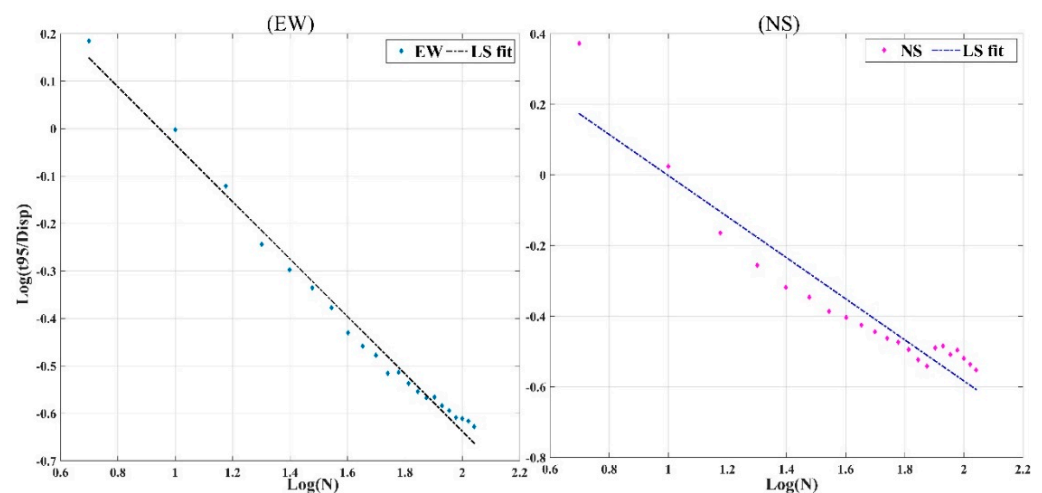
#### 4.7. Analysis of Final Velocity Directions

Figure 13A shows the vector fields of dune migration at the NSSS, with most vectors toward the east, consistent with previous reports of prevailing wind directions over Sinai. However, at some locations (i.e., east of the Suez Canal, the red rectangle in Figure 13A), the migration directions were south and southeast. These results are also consistent with previous reports of migration directions to the east of the Suez Canal [21]. Consistent with the complexity of the wind regime in the NSSS, such variability in migration directions between individual matching measurements was to be expected. To better assess the consistency of the directions, the VVC was extracted, as shown in Figure 13B. Poor consis-

tency can be observed over stable targets, which can be attributed to the co-registration residual. In contrast, the VVC over dune targets showed good consistency, which is a good indicator of the lowest degree of divergence of directions between individual velocities. The higher VVC denoted a large consistency of the direction extracted from the individual pairs. Figure 14 shows the sand roses of the final velocities from Landsat-8 of the points shown in Figure 1. The predominant directions of all points show a tendency to migrate to the north and northeast, except for point (F) (near Bitter Lake), where the direction of migration is to the south. The CR values of the active dune features associated with each region used for sand rose extraction ranged from 0.859 (point G) to 0.987 (point F). Higher values of CR denote the homogeneity of the directions used to estimate the average directions. With the exception of two stations (Bir-Elabd and El-Malease), where we relied on Ali et al.'s [25] reports of wind records for the three years from 2013 to 2015, we also have old wind records in the format of monthly average values for three metrological stations (see Table S2). We used the wind records, applying Fryberger's equation [53] to estimate the drift potential (DP) and the resultant drift direction (RDD), with the threshold velocity set to 4 m/s according to the previous reports of Reference [48]. For the wind records available in a monthly average format, we estimated the average RDD of each season and the corresponding CR, while, for the average annual records, we estimated the average RDD of the three available years. The average migration directions of each region extracted from the final velocities, the corresponding CR of each region, and the RDD at the location of the meteorological stations are shown in Table S2.



**Figure 9.** The dispersion of the final velocity (i.e., median velocity). The dispersions for: (A) zone A, (B) zone B, and (C) zone C.



**Figure 10.** The linear relationship between the logarithm of the ratio between the 95% confidence interval of the records  $t_{95}$  and the dispersion (y-axis), and the number of individual velocities shared in estimating the final velocity (x-axis).

For points B and F (see Figure 1), the differences between the prevailing directions extracted by Landsat-8 and Sentinel-2 were about  $12^\circ$  and  $0^\circ$ , respectively. The large difference at point B can be attributed to the different observation periods of Landsat-8 and Sentinel-2. However, almost no difference was observed at point F, regardless of the observation period, which can be attributed to the spatiotemporal variability of wind speeds and directions over the Sand Sea. The median VVC in the regions around points B and F were 0.72 and 0.89, respectively, providing an indication of the variability in the directions between the individual maps used in the fusion of the final velocities. A higher VVC value at point F can be considered as an indicator of the homogeneity of the velocity directions estimated from the individual maps and can therefore interpret the zero difference between the prevailing directions between Landsat-8 and Sentinel-2. The RDD values estimated from the wind data showed large differences between different seasons at the same metrological station. Moreover, the RDD also varied spatially between different metrological stations. Temporally, it was observed that the RDD varied between the old and current wind records. The above observations are in agreement with previous reports on the spatiotemporal variability of wind regimes over sand seas [21]. This would also support the differences between the prevailing directions extracted from Landsat-8 and Sentinel-2, especially at EL-Malease Station (point B). Moreover, differences between the matching results and the RDD values are expected. However, we found that the difference between the RDD estimated from recent wind data (i.e., 2013–2015) and the prevailing directions obtained from Landsat-8 at Bir El-Abd Station was about four degrees. The preceding discussion demonstrated the inhomogeneous nature of the wind regimes in the NSSS and supported the potential of the prevailing directions obtained from the fusion of the individual matching results.

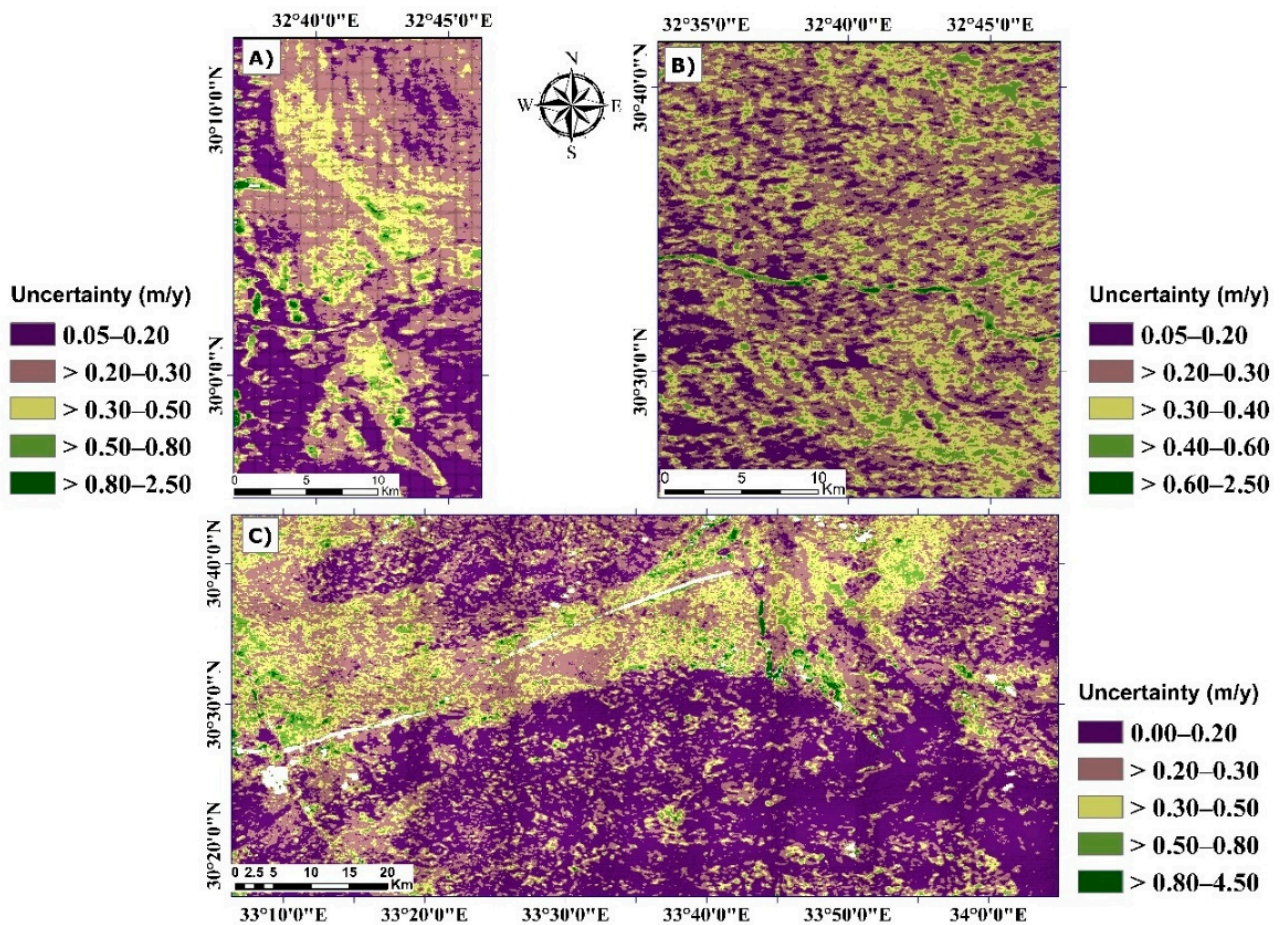


**Figure 11.** The uncertainty of the final velocity (i.e., median velocity). The uncertainty for: (A) zone A, (B) zone B, and (C) zone C.

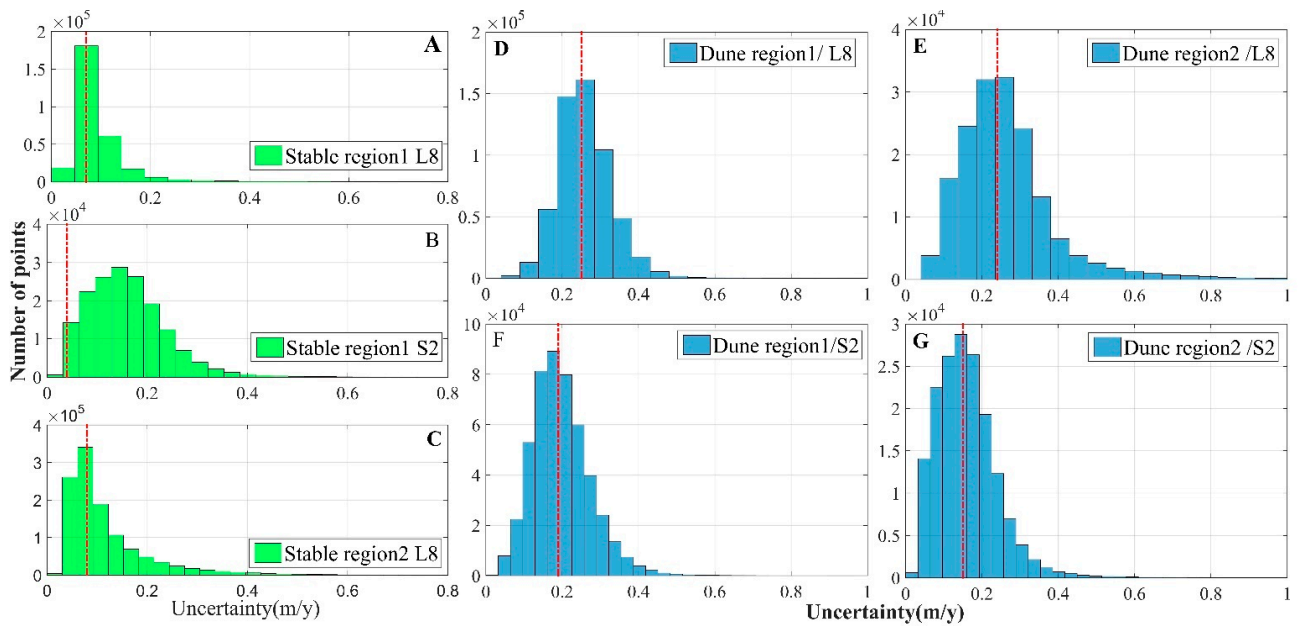


**Figure 12.** The histograms of the uncertainty distributions for the stable and moving targets. (A–C) The histogram of the uncertainty distributions of stable regions 1 and 2. (D,F) The Landsat-8 uncertainty distributions over the moving targets of regions 1 and 2, respectively. (E,G) The same as (D) and (F) but for Sentinel-2. The red dashed lines represent the median of each distribution.

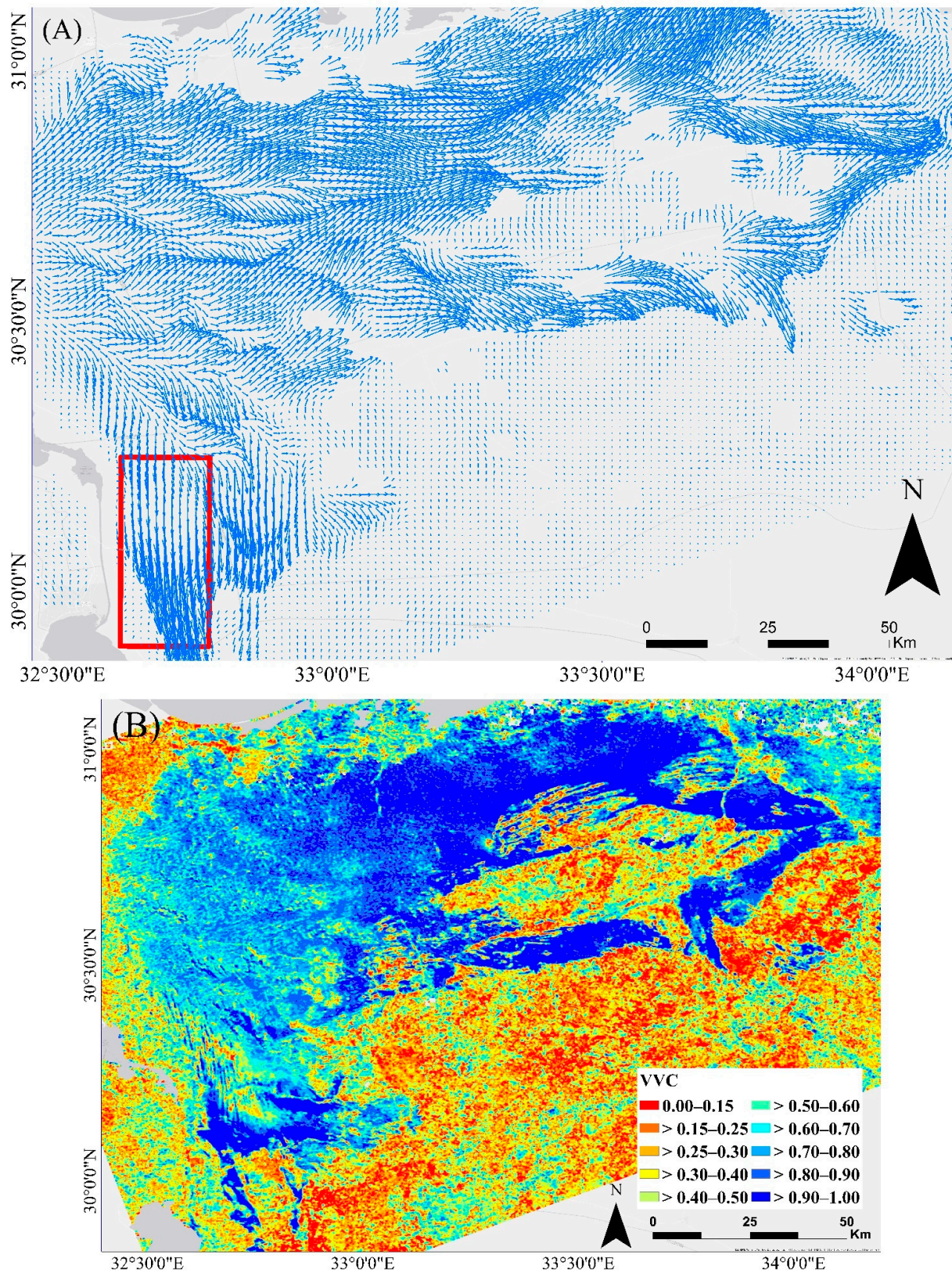


**Figure 13.** (A) The dominant migration directions covering the entire NSSS displayed as vector fields. These vector fields were extracted from the add-in module in COSI-Corr. This map was generated by setting 100 and 25 pixels as the sliding and step window size, respectively. The red rectangle outlines the area where the dune migration is toward the south. (B) The VVC of the velocity directions. The background is Google Earth Image © using Esri ArcMap 10.3.

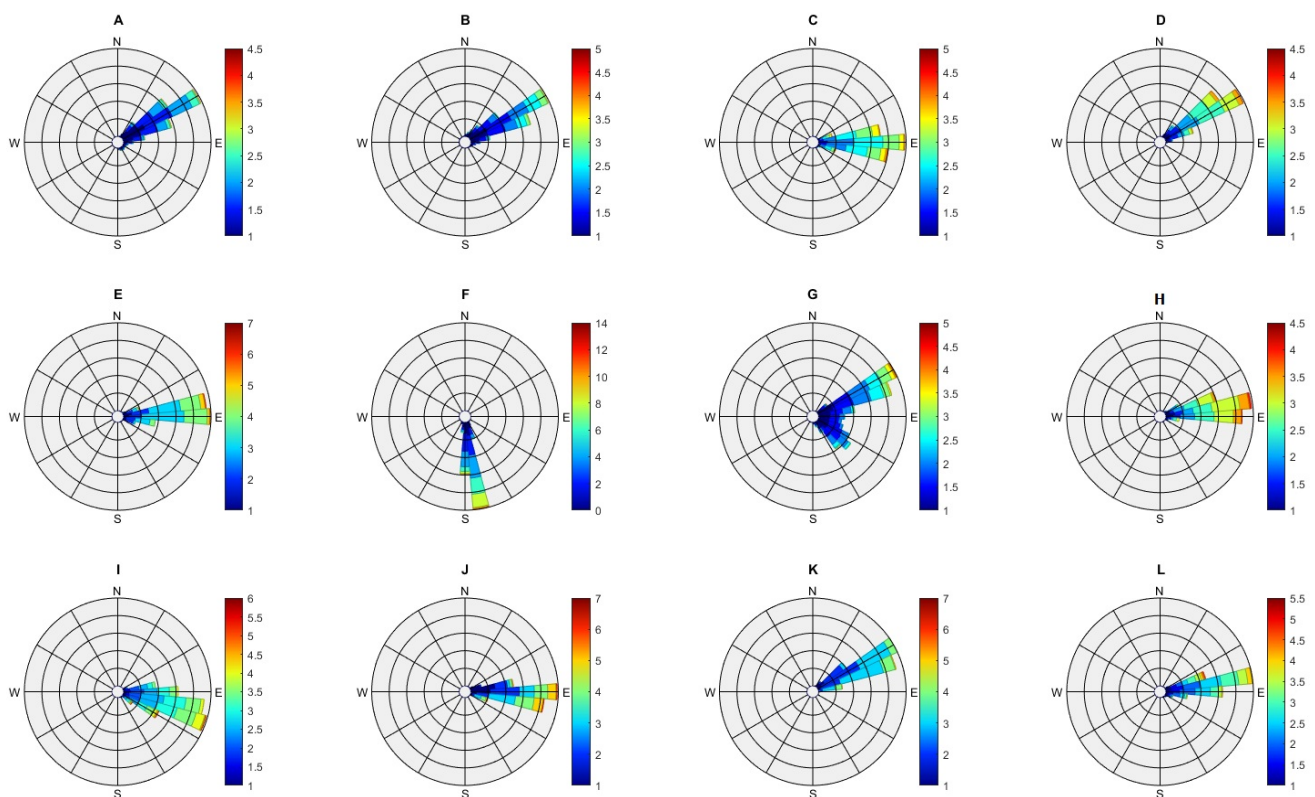


**Figure 14.** (A–L) Sand roses extracted from the final velocity of Landsat-8 over different localities in the NSSS. The different letters denote the different locations displayed in Figure 1. Units are in m/y. The coordinates of the points are attached in Table S2.

## 5. Discussion

### 5.1. Spatiotemporal Variability of Dune Velocities

Dune velocities in the NSSS are characterized by spatial and temporal variabilities due to differences in the activities of the effective winds, the sand supply, and the vegetation cover. To better account for the variability in estimated dune velocities between pairs, we extracted six regions distributed across different locations in the NSSS (see Figure 1). Pixels with velocities less than 0.5 m/y were discarded and considered interdune regions. We estimated the geometric mean for all the surviving pixels belonging to the selected regions for each pair. Figure 15A shows whisker box plots illustrating the variability in active dune velocities between the different pairs. In addition, we clipped the final velocity (i.e., the mean velocity) in the six regions and similarly estimated the geometric mean, as shown in Figure 15B. It is noticeable that the geometric mean estimated from the final velocity of the six regions showed lower values than the median of the geometric mean of the individual pairs; however, almost the same trend was observed. It was observed that region 2 (east of the Suez Canal) recorded the highest median of 3.0 m/y, revealing the highest dune activity across the NSSS. It was reported that the dunes on the Sinai side were relatively more active than those on the Negev side, while the Negev side appeared darker than the Egyptian side [1,3]. On the Egyptian side, there were activities that affected the vegetation cover, such as overgrazing, wood grazing, and trampling, while these activities were mainly prohibited on the Negev side [3]. Regions 5 and 6 are located east and west of the Sinai-Negev boundary, respectively. It is noted that the median of the geometric mean of regions 5 and 6 had almost similar values around 1.5 m/, regardless the relative stability of the dunes in the Negev side, as reported by previous studies [1,3]. This could be due

to the fact that the medium resolution images had problems in distinguishing between vegetation and sand, while such small details regarding dune activities can be achieved with high-resolution images.

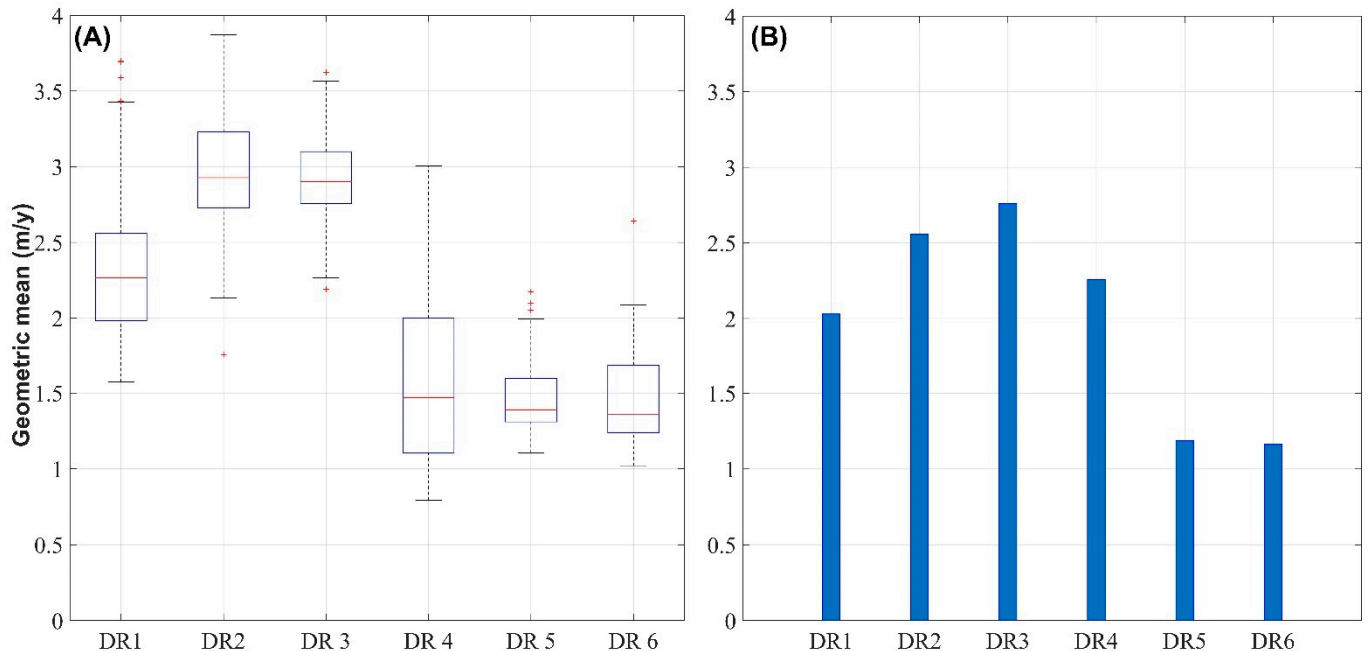


**Figure 15.** (A) Whisker box plots highlighting the variability of the geometric mean of the annual rates extracted for six regions. The red horizontal lines represent the median value, wherein the red points refer to the outliers. (B) Bar chart representing the median of the geometric mean of the final velocity (i.e., the median velocity) for the six regions.

### 5.2. Comparison between the Combined Velocites and Individual Velocites

To evaluate the contribution of the fusion process, we compared the results extracted from the individual velocities and from the fusion process for the Landsat-8 image (P/175, R/39) in terms of the MAD over stable targets and the SRs recorded over moving targets. Figure 16A shows the SR values of each pair and the final velocity. It can be observed that the SRs ranged from 40% to 97%, with the SR of the fusion being almost 100% for both median and inversion fusion. Figure 16B shows the MAD values of the individual pairs, where the MAD ranged from 0.18 to 1.3 m/y. Similarly, the values for the fusion process were 0.37 and 0.48 m/y for inversion and median fusion, respectively. Remarkably, the MAD of the fusion was not the lowest compared to the individual pairs; this can be attributed to the quality of the individual pairs due to the selection procedure, the filtering process, and the improvement in the co-registration and orthorectification accuracy for Landsat-8. Comparatively, the fusion performed by Dehecq et al. [42] with the archives of Landsat (5/7) showed an average value of MAD of 5.5 m/y, which was reduced to 1.4 m/y by the fusion. The comparison between the fusion of Landsat-8 and Landsat (5/7) showed an improved performance of Landsat-8, with a MAD final velocity four times lower than before.

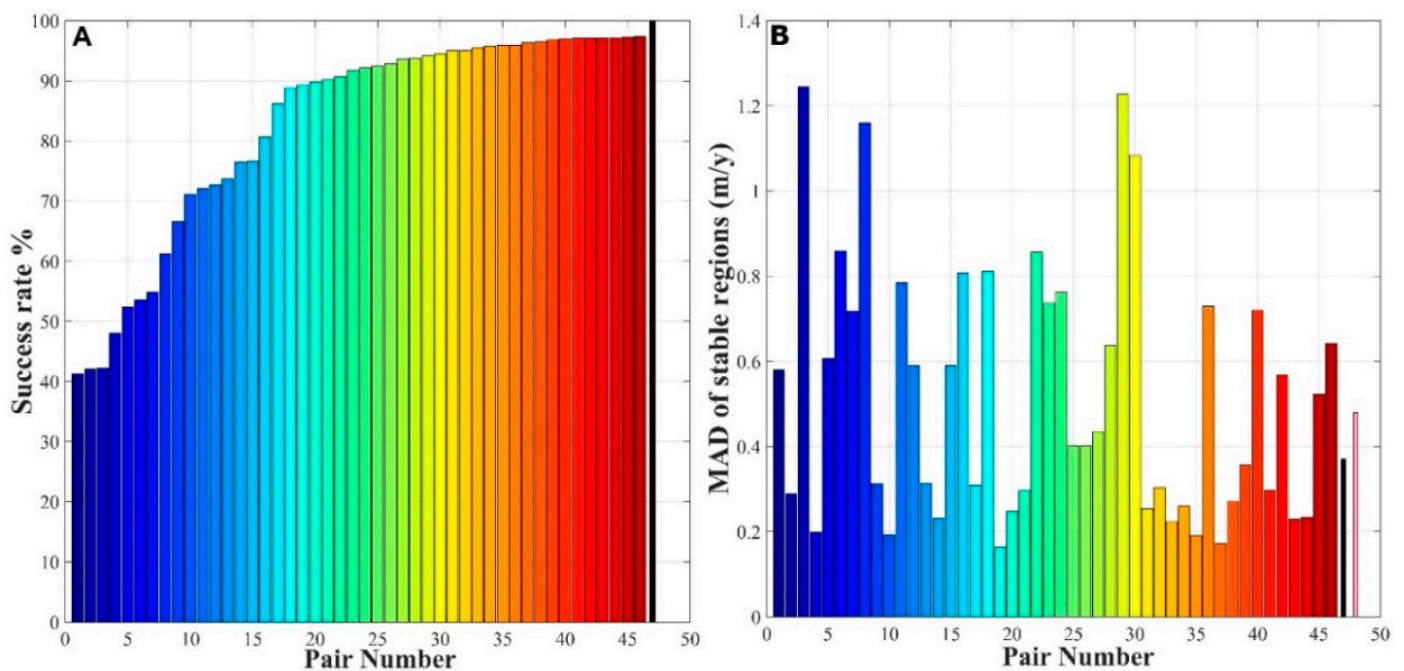


**Figure 16.** (A) SR comparison between the individual pairs and the fusion; the pairs were arranged according to the values of the SRs; the black bar denotes the SR of the fusion. (B) The MAD of stable targets of the individual pairs and of the fusion (the black and rose bars represent inversion and median fusion, respectively).

## 6. Conclusions

In this study, we introduced a complete coverage of dune velocities and corresponding uncertainties in the NSSS. The dynamics of dunes are closely coupled to the complex nature of the wind regime, where the wind speed and direction vary spatially and temporally. Accordingly, the migration rates are expected to change between the individual matching maps. To increase the reliability of the introduced dune velocities, we first selected pairs with smaller variations in the solar angle and with at least one-year time separation. We then combined the individual maps to determine the final velocity. The fusion allowed us to cover about 98.8% of the dune area in the NSSS. To estimate the uncertainty in the final velocity, we used the velocities over a stable region to calibrate the relationship between the number of individual maps and the dispersion. After the calibration, we used the extracted models to estimate the 95% confidence interval of the final velocity for each velocity location. The median of the uncertainties of the stable targets for both Landsat-8 and Sentinel-2 showed that the co-registration accuracy improved for both satellites compared to previous missions (e.g., Landsat 5/7). Owing to the paucity of field measurements, we compared the final velocity of Landsat-8 with that of Sentinel-2. The correlation between the Landsat-8 and Sentinel-2 velocities reached a maximum of 89%, and the median absolute velocity difference was of the order of 0.50 m/y. The directions extracted from the fusion showed good agreement with the RDD extracted from the wind records. The VVC extracted from the fusion provided new insights into understanding the complex spatiotemporal patterns of dune migration directions in the NSSS. The fusion enabled the large-scale monitoring of the spatiotemporal variability of the dune velocities in the NSSS with high spatial coverage and lower uncertainties. This method is highly recommended for monitoring dune velocities at the dune field scale and is considered an indicator of the dune activity status over a certain period.

**Supplementary Materials:** The following are available online at <https://www.mdpi.com/article/10.3390/rs13183694/s1>: Table S1: Information on the Landsat-8 and Sentinel-2 images used in this study. Table S2: Prevailing migration directions extracted from the optical matching results and the resultant drift directions extracted from the wind records.

**Author Contributions:** Conceptualization, E.A. and W.X.; Formal analysis, E.A.; Investigation, E.A.; Methodology, E.A.; Project administration, W.X.; Resources, X.D.; Supervision, W.X. and X.D.; Validation, E.A.; Visualization, E.A.; Writing—original draft, E.A.; and Writing—review and editing, E.A. and W.X. All authors have read and agreed to the published version of the manuscript.

**Funding:** This research was supported by the National Natural Science Foundation of China under grant no. 41804015 and the National Key R&D Program of China (2019YFC1509205).

**Institutional Review Board Statement:** Not applicable.

**Informed Consent Statement:** Not applicable.

**Acknowledgments:** We are very thankful to ESA for the provision of the Copernicus Sentinel-2 data through the Sentinel Science Hub and Sentinel-2 Expert Users Data Hub, the USGS for the provision of the Landsat data through Earth Explorer <http://earthexplorer.usgs.gov/>, accessed on 10 September 2021, and the Caltech group for providing COSI-Corr. We used Arc Map 10.3 software for the spatial analysis and map generation. Additionally, we used MATLAB 2016a for coding and scripting. This research was jointly supported by the Research Grants Council (RGC) of the Hong Kong Special Administrative Region (PolyU 152232/17E, PolyU 152164/18E, and PolyU 152233/19E); the Research Institute for Sustainable Urban Development (RISUD); Hong Kong Polytechnic University; and the Innovative Technology Fund (ITP/019/20LP).

**Conflicts of Interest:** The authors declare no conflict of interest.

## References

1. Hugenholtz, C.H.; Levin, N.; Barchyn, T.E.; Baddock, M.C. Remote sensing and spatial analysis of aeolian sand dunes: A review and outlook. *Earth Sci. Rev.* **2012**, *111*, 319–334. [[CrossRef](#)]
2. Scheidt, S.P.; Lancaster, N. The application of COSI-Corr to determine dune system dynamics in the southern Namib Desert using ASTER data. *Earth Surf. Process. Landf.* **2013**, *38*, 1004–1019. [[CrossRef](#)]
3. Ashkenazy, Y.; Shilo, E. Sand dune Albedo feedback. *Geosciences* **2018**, *8*, 83. [[CrossRef](#)]
4. Effat, H.; Hegazy, M.; Behr, F. Cartographic Modeling of Potential Sand Dunes Movement Risk Using Remote Sensing and Geographic Information System in Sinai, Egypt. In *Landuse/Landcover of Sialkot Using RS & GIS—An Urban Sprawl Perspective*; AGSE Publishing: Karlsruhe, Germany, 2012; pp. 139–148.
5. Hamdan, M.A.; Refaat, A.A.; Abdel Wahed, M. Morphologic characteristics and migration rate assessment of barchan dunes in the Southeastern Western Desert of Egypt. *Geomorphology* **2016**, *257*, 57–74. [[CrossRef](#)]
6. Ahmady-Birgani, H.; McQueen, K.G.; Moeinaddini, M.; Naseri, H. Sand Dune Encroachment and Desertification Processes of the Rigboland Sand Sea, Central Iran. *Sci. Rep.* **2017**, *7*, 1523. [[CrossRef](#)]
7. Ding, C.; Zhang, L.; Liao, M.; Feng, G.; Dong, J.; Ao, M.; Yu, Y. Quantifying the spatio-temporal patterns of dune migration near Minqin Oasis in northwestern China with time series of Landsat-8 and Sentinel-2 observations. *Remote Sens. Environ.* **2020**, *236*, 111498. [[CrossRef](#)]
8. Lam, D.K.; Rimmel, T.K.; Drezner, T.D. Tracking desertification in California using remote sensing: A sand dune encroachment approach. *Remote Sens.* **2011**, *3*, 1–13. [[CrossRef](#)]
9. Ding, C.; Feng, G.; Liao, M.; Zhang, L. Change detection, risk assessment and mass balance of mobile dune fields near Dunhuang Oasis with optical imagery and global terrain datasets. *Int. J. Digit. Earth* **2020**, *13*, 1604–1623. [[CrossRef](#)]
10. Ghadir, M.; Shalaby, A.; Koch, B. A new GIS-based model for automated extraction of Sand Dune encroachment case study: Dakhla Oases, western desert of Egypt. *Egypt. J. Remote Sens. Sp. Sci.* **2012**, *15*, 53–65. [[CrossRef](#)]
11. Ali, M.; Latif, A.; Elhag, M.M. Combating Desertification in Sudan. In *Environment and Ecology at the Beginning of 21st Century*; St. Kliment Ohridski University Press: Sofia, Bulgaria, 2015; Chapter 18; pp. 256–266.
12. Baird, T.; Bristow, C.; Vermeesch, P. Measuring Sand Dune Migration Rates with COSI-Corr and Landsat: Opportunities and Challenges. *Remote Sens.* **2019**, *11*, 2423. [[CrossRef](#)]
13. Mohamed, I.N.L.; Verstraeten, G. Analyzing dune dynamics at the dune-field scale based on multi-temporal analysis of Landsat-TM images. *Remote Sens. Environ.* **2012**, *119*, 105–117. [[CrossRef](#)]
14. Potter, C.; Weigand, J. Analysis of Desert Sand Dune Migration Patterns from Landsat Image Time Series for The Southern California Desert. *J. Remote Sens. GIS* **2016**, *5*, 1–8. [[CrossRef](#)]
15. Levin, N.; Ben-Dor, E.; Karnieli, A. Topographic information of sand dunes as extracted from shading effects using Landsat images. *Remote Sens. Environ.* **2004**, *90*, 190–209. [[CrossRef](#)]
16. Ali, E.; Xu, W. An optical image time series inversion method and application to long term sand dune movements in the Sinai Peninsula. In *Proceedings of the European Geosciences Union (EGU), Vienna, Austria, 7–12 April 2019*.
17. Vermeesch, P.; Leprince, S. A 45-year time series of dune mobility indicating constant windiness over the central Sahara. *Geophys. Res. Lett.* **2012**, *39*. [[CrossRef](#)]

18. Vermeesch, P.; Drake, N. Remotely sensed dune celerity and sand flux measurements of the world's fastest barchans (Bodélé, Chad). *Geophys. Res. Lett.* **2008**, *35*, 1–6. [[CrossRef](#)]
19. Necsoiu, M.; Leprince, S.; Hooper, D.M.; Dinwiddie, C.L.; McGinnis, R.N.; Walter, G.R. Monitoring migration rates of an active subarctic dune field using optical imagery. *Remote Sens. Environ.* **2009**, *113*, 2441–2447. [[CrossRef](#)]
20. Hermas, E.S.; Alharbi, O.; Alqurashi, A.; Niang, A.J.; Al-Ghamdi, K.; Al-Mutiry, M.; Farghaly, A. Characterisation of sand accumulations in Wadi Fatmah and Wadi Ash Shumaysi, KSA, Using multi-source remote sensing imagery. *Remote Sens.* **2019**, *11*, 2824. [[CrossRef](#)]
21. Hermas, E.; Leprince, S.; El-Magd, I.A. Retrieving sand dune movements using sub-pixel correlation of multi-temporal optical remote sensing imagery, northwest Sinai Peninsula, Egypt. *Remote Sens. Environ.* **2012**, *121*, 51–60. [[CrossRef](#)]
22. Al-Ghamdi, K.; Hermas, E. Assessment of dune migration hazards against landuse northwest Al-lith City, Saudi Arabia, using multi-temporal satellite imagery. *Arab. J. Geosci.* **2015**, *8*, 11007–11018. [[CrossRef](#)]
23. Al-Mutiry, M.; Hermas, E.A.; Al-Ghamdi, K.A.; Al-Awaji, H. Estimation of dune migration rates north Riyadh City, KSA, using SPOT 4 panchromatic images. *J. Afr. Earth Sci.* **2016**, *124*, 258–269. [[CrossRef](#)]
24. Els, A.; Merlo, S.; Knight, J. Comparison of two Satellite Imaging Platforms for Evaluating Sand Dune Migration in the Ubari Sand Sea (Libyan Fazzan). *Int. Arch. Photogramm. Remote. Sens. Spat. Inf. Sci.* **2015**, *40*, 1375–1380. [[CrossRef](#)]
25. Ali, E.; Xu, W.; Ding, X. Improved optical image matching time series inversion approach for monitoring dune migration in North Sinai Sand Sea: Algorithm procedure, application, and validation. *ISPRS J. Photogramm. Remote Sens.* **2020**, *164*, 106–124. [[CrossRef](#)]
26. Dong, P. Automated measurement of sand dune migration using multi-temporal lidar data and GIS. *Int. J. Remote Sens.* **2015**, *36*, 5426–5447. [[CrossRef](#)]
27. Dong, P.; Xia, J.; Zhong, R.; Zhao, Z.; Tan, S. A New Method for Automated Measurement of Sand Dune Migration Based on Multi-Temporal LiDAR-Derived Digital Elevation Models. *Remote Sens.* **2021**, *13*, 3084. [[CrossRef](#)]
28. Grohmann, C.H.; Garcia, G.P.B.; Affonso, A.A.; Albuquerque, R.W. Dune migration and volume change from airborne LiDAR, terrestrial LiDAR and Structure from Motion-Multi View Stereo. *Comput. Geosci.* **2020**, *143*, 104569. [[CrossRef](#)]
29. Pagán, J.I.; Bañón, L.; López, I.; Bañón, C.; Aragonés, L. Monitoring the dune-beach system of Guardamar del Segura (Spain) using UAV, SfM and GIS techniques. *Sci. Total Environ.* **2019**, *687*, 1034–1045. [[CrossRef](#)]
30. Laporte-Fauret, Q.; Marieu, V.; Castelle, B.; Michalet, R.; Bujan, S.; Rosebery, D. Low-Cost UAV for high-resolution and large-scale coastal dune change monitoring using photogrammetry. *J. Mar. Sci. Eng.* **2019**, *7*, 63. [[CrossRef](#)]
31. Leprince, S.; Barbot, S.; Ayoub, F.; Avouac, J.-P. Automatic and Precise Orthorectification, Coregistration, and Subpixel Correlation of Satellite Images, Application to Ground Deformation Measurements. *IEEE Geosci. Remote Sens. Lett.* **2007**, *45*, 1529–1558. [[CrossRef](#)]
32. Sam, L.; Gahlot, N.; Prusty, B.G. Estimation of dune celerity and sand flux in part of West Rajasthan, Gadra area of the Thar Desert using temporal remote sensing data. *Arab. J. Geosci.* **2015**, *8*, 295–306. [[CrossRef](#)]
33. Bridges, N.T.; Ayoub, F.; Avouac, J.; Leprince, S.; Lucas, A.; Mattson, S. Earth-like sand fluxes on Mars. *Nature* **2012**, *485*, 339–342. [[CrossRef](#)] [[PubMed](#)]
34. Ayoub, F.; Avouac, J.-P.; Newman, C.E.; Richardson, M.I.; Lucas, A.; Leprince, S.; Bridges, N.T. Threshold for sand mobility on Mars calibrated from seasonal variations of sand flux. *Nat. Commun.* **2014**, *5*, 5096. [[CrossRef](#)]
35. Davis, J.M.; Grindrod, P.M.; Boazman, S.J.; Vermeesch, P.; Baird, T. Quantified Aeolian Dune Changes on Mars Derived From Repeat Context Camera Images. *Earth Sp. Sci.* **2020**, *7*, e2019EA000874. [[CrossRef](#)]
36. Kääb, A.; Winsvold, S.; Altena, B.; Nuth, C.; Nagler, T.; Wuite, J. Glacier Remote Sensing Using Sentinel-2. Part I: Radiometric and Geometric Performance, and Application to Ice Velocity. *Remote Sens.* **2016**, *8*, 598. [[CrossRef](#)]
37. Fahnestock, M.; Scambos, T.; Moon, T.; Gardner, A.; Haran, T.; Klinger, M. Rapid large-area mapping of ice flow using Landsat 8. *Remote Sens. Environ.* **2016**, *185*, 84–94. [[CrossRef](#)]
38. Bontemps, N.; Lacroix, P.; Doin, M. Inversion of deformation fields time-series from optical images, and application to the long term kinematics of slow-moving landslides in Peru. *Remote Sens. Environ.* **2018**, *210*, 144–158. [[CrossRef](#)]
39. Ding, C.; Feng, G.; Li, Z.; Shan, X.; Du, Y.; Wang, H. Spatio-Temporal Error Sources Analysis and Accuracy Improvement in Landsat 8 Image Ground Displacement Measurements. *Remote Sens.* **2016**, *8*, 937. [[CrossRef](#)]
40. Leprince, S.; Member, S.; Musé, P.; Avouac, J. In-Flight CCD Distortion Calibration for Pushbroom Satellites Based on Subpixel Correlation. *IEEE Geosci. Remote Sens. Lett.* **2008**, *46*, 2675–2683. [[CrossRef](#)]
41. Lacroix, P.; Bièvre, G.; Pathier, E.; Kniess, U.; Jongmans, D. Use of Sentinel-2 images for the detection of precursory motions before landslide failures. *Remote Sens. Environ.* **2018**, *215*, 507–516. [[CrossRef](#)]
42. Dehecq, A.; Gourmelen, N.; Trouve, E. Deriving large-scale glacier velocities from a complete satellite archive: Application to the Pamir-Karakoram-Himalaya. *Remote Sens. Environ.* **2015**, *162*, 55–66. [[CrossRef](#)]
43. Mouginot, J.; Rignot, E.; Scheuchl, B.; Millan, R. Comprehensive annual ice sheet velocity mapping using Landsat-8, Sentinel-1, and RADARSAT-2 data. *Remote Sens.* **2017**, *9*, 364. [[CrossRef](#)]
44. Millan, R.; Mouginot, J.; Rabatel, A.; Jeong, S.; Cusicanqui, D.; Derkacheva, A.; Chekki, M. Mapping surface flow velocity of glaciers at regional scale using a multiple sensors approach. *Remote Sens.* **2019**, *11*, 2498. [[CrossRef](#)]
45. Derkacheva, A.; Mouginot, J.; Millan, R.; Maier, N.; Gillet-Chaulet, F. Data reduction using statistical and regression approaches for ice velocity derived by Landsat-8, Sentinel-1 and Sentinel-2. *Remote Sens.* **2020**, *12*, 1935. [[CrossRef](#)]

46. Bubenzer, O.; Embabi, N.S.; Ashour, M.M. Sand seas and dune fields of Egypt. *Geosciences* **2020**, *10*, 101. [[CrossRef](#)]
47. Embabi, N.S. *Landscapes and Landforms of Egypt: World Geomorphological Landscapes*; Springer: Berlin/Heidelberg, Germany, 2018; ISBN 978-3-319-65659-5.
48. ElBanna, M.S. Geological Studies Emphasizing the Morphology and Dynamics of Sand Dunes and their Environmental Impacts on the Reclamation and Developmental Areas in Northwest Sinai, Egypt. Ph.D. Thesis, Cairo University, Cairo, Egypt, 2004.
49. Scherler, D.; Leprince, S.; Strecker, M.R. Glacier-surface velocities in alpine terrain from optical satellite imagery—Accuracy improvement and quality assessment. *Remote Sens. Environ.* **2008**, *112*, 3806–3819. [[CrossRef](#)]
50. Paul, F.; Bolch, T.; Briggs, K.; Kääb, A.; McMillan, M.; McNabb, R.; Nagler, T.; Nuth, C.; Rastner, P.; Strozzi, T.; et al. Error sources and guidelines for quality assessment of glacier area, elevation change, and velocity products derived from satellite data in the Glaciers\_cci project. *Remote Sens. Environ.* **2017**, *203*, 256–275. [[CrossRef](#)]
51. Shukla, A.; Garg, P.K. Spatio-temporal trends in the surface ice velocities of the central Himalayan glaciers, India. *Glob. Planet. Chang.* **2020**, *190*, 103187. [[CrossRef](#)]
52. Stumpf, A.; Malet, J.P.; Delacourt, C. Correlation of satellite image time-series for the detection and monitoring of slow-moving landslides. *Remote Sens. Environ.* **2017**, *189*, 40–55. [[CrossRef](#)]
53. Fryberger, S.G. Mechanisms for the formation of eolian sand seas. *Zeitschrift für Geomorphol. Ann. Geomorphol. Ann. Géomorphologie* **1979**, *23*, 440–460.